

Voxelized ray-tracing simulation dedicated to multi-pinhole molecular breast tomosynthesis

Wang, Beien; Van Roosmalen, Jarno; Piët, Louis; VanSchie, Marcel A.; Beekman, Freek J.; Goorden, Marlies C.

DOI

[10.1088/2057-1976/aa8012](https://doi.org/10.1088/2057-1976/aa8012)

Publication date

2017

Document Version

Final published version

Published in

Biomedical Physics & Engineering Express

Citation (APA)

Wang, B., Van Roosmalen, J., Piët, L., VanSchie, M. A., Beekman, F. J., & Goorden, M. C. (2017). Voxelized ray-tracing simulation dedicated to multi-pinhole molecular breast tomosynthesis. *Biomedical Physics & Engineering Express*, 3(4), Article 045021. <https://doi.org/10.1088/2057-1976/aa8012>

Important note

To cite this publication, please use the final published version (if applicable).
Please check the document version above.

Copyright

Other than for strictly personal use, it is not permitted to download, forward or distribute the text or part of it, without the consent of the author(s) and/or copyright holder(s), unless the work is under an open content license such as Creative Commons.

Takedown policy

Please contact us and provide details if you believe this document breaches copyrights.
We will remove access to the work immediately and investigate your claim.



PAPER

Voxelized ray-tracing simulation dedicated to multi-pinhole molecular breast tomosynthesis

To cite this article: Beien Wang *et al* 2017 *Biomed. Phys. Eng. Express* **3** 045021

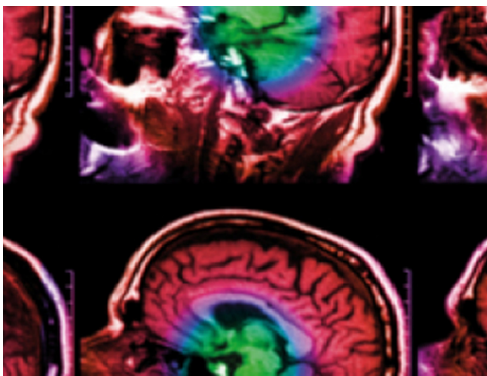
View the [article online](#) for updates and enhancements.

Related content

- [Molecular breast tomosynthesis with scanning focus multi-pinhole cameras](#)
Jarno van Roosmalen, Marlies C Goorden and Freek J Beekman
- [System geometry optimization for molecular breast tomosynthesis with focusing multi-pinhole collimators](#)
Jarno van Roosmalen, Freek J Beekman and Marlies C Goorden
- [Comparison of fan beam, slit-slat and multi-pinhole collimators for molecular breast tomosynthesis](#)
Jarno van Roosmalen, Freek J Beekman and Marlies C Goorden

Recent citations

- [Characterization of a multi-pinhole molecular breast tomosynthesis scanner](#)
Beien Wang *et al*
- [Accelerated image reconstruction by a combined dual-matrix dual-voxel approach](#)
Marlies C Goorden *et al*
- [Optimized sampling for high resolution multi-pinhole brain SPECT with stationary detectors](#)
Yuan Chen *et al*



IPEM | IOP

Series in Physics and Engineering in Medicine and Biology

Your publishing choice in medical physics,
biomedical engineering and related subjects.

Start exploring the collection—download the
first chapter of every title for free.

Biomedical Physics & Engineering Express



PAPER

Voxelized ray-tracing simulation dedicated to multi-pinhole molecular breast tomosynthesis

RECEIVED
28 February 2017

REVISED
13 June 2017

ACCEPTED FOR PUBLICATION
17 July 2017

PUBLISHED
26 July 2017

Beien Wang^{1,3,4}, Jarno van Roosmalen^{1,3}, Louis Piët¹, Marcel A van Schie¹, Freek J Beekman^{1,2} and Marlies C Goorden¹

¹ Section of Radiation, Detection and Medical Imaging, Faculty of Applied Sciences, Delft University of Technology, Mekelweg 15, 2629 JB Delft, The Netherlands

² MILabs B.V., Heidelberglaan 100, 3584 CX, Utrecht, The Netherlands

³ Beien Wang and Jarno van Roosmalen have contributed equally to this work.

⁴ Author to whom any correspondence should be addressed.

E-mail: b.wang-1@tudelft.nl

Keywords: breast imaging, SPECT, Monte Carlo simulation, raytracing, pinhole collimator

Supplementary material for this article is available [online](#)

Abstract

Accurate gamma photon transport simulations of emission tomography systems are important to optimise system geometries and for iterative image reconstruction. Monte Carlo simulation (MCS) is widely established for this purpose but has the disadvantage of being prohibitively slow. Voxelized ray tracing (VRT) can be used as an alternative but the accuracy of VRT needs to be assessed for each simulation task at hand. The aim of this work is to propose and validate a dedicated VRT code for a novel radionuclide-based multi-pinhole molecular breast tomosynthesis (MP-MBT) scanner. The MP-MBT system images radionuclide distributions in a mildly compressed breast using two opposing gamma cameras, each equipped with a focusing multi-pinhole collimator, that slide along opposite sides of the breast. VRT simulates gamma photon transport by tracing rays efficiently through the voxelized phantom, collimator, and detector volumes using Siddon's raytracing algorithm, accelerated by dual-grid methods. To assess its accuracy, we compare point spread functions (PSFs) calculated with VRT for different voxel sizes with those generated by the established MCS toolkit GATE. Furthermore, VRT and MCS-simulated projections of realistic anthropomorphic XCAT phantoms with different compressed breast sizes are compared, as well as reconstructed images obtained from these projections. With VRT, PSFs for MP-MBT can be simulated accurately when the fine voxel size of the VRT's dual-grid is 1/8 mm. Reaching a similar deviation from noiseless PSFs takes 29 300 times longer with full MCS than with VRT. Furthermore, XCAT phantom simulations show that VRT-generated projections are very close to MCS-generated low-noise projections when these are corrected for scatter by the triple energy window method. However, we also find that primary gamma photons from the torso may in some cases reach the detector, meaning that torso activity should not be neglected in VRT. Finally, reconstructed images obtained from projections generated by VRT and MCS are visually very similar and have no significant difference in contrast and noise characteristics. We conclude that VRT can accurately and efficiently simulate MP-MBT even though it neglects scattered photons originating from the torso.

1. Introduction

Imaging of radiolabelled molecule distributions is gaining popularity for breast cancer diagnosis. Recently, several breast-specific gamma cameras have been proposed and significant advances in the sensitivity of these cameras have been made (Mueller *et al* 2003, Coover *et al* 2004,

Hruska *et al* 2008c, 2012a, 2012b, Siman and Kappadath 2012, Long *et al* 2016). Alongside these planar gamma cameras, there is also growing interest in 3D molecular breast imaging. General purpose single photon emission computed tomography (SPECT) and positron emission tomography (PET) are not ideal for breast imaging because they often provide no higher diagnostic

sensitivity and specificity than planar systems (Hruska and O'Connor 2013, Fowler 2014). Therefore, dedicated 3D molecular breast imaging techniques are being investigated (Tornai *et al* 2003, Brzymialkiewicz *et al* 2005, Raylman *et al* 2008, MacDonald *et al* 2009, Baghaei *et al* 2010, Williams *et al* 2010, Yanagida *et al* 2010, Moliner *et al* 2012, Gopan *et al* 2014, Gong and Williams 2015). Recently, we proposed dedicated molecular breast tomosynthesis based on sliding multi-pinhole collimators, known as MP-MBT (Beekman 2011, van Roosmalen *et al* 2016).

To investigate the performance of MP-MBT and to further optimize its design, acquisition, and reconstruction parameters, efficient simulation algorithms are useful. To be able to evaluate images that could be acquired with MP-MBT, one has to be able to generate both noisy ensembles of projections of realistic distributions, as well as the virtually noiseless point spread functions (PSFs, the detector's response to a point source of activity) that are used in image reconstruction. Monte Carlo simulation (MCS) is a powerful technique for assessing gamma photon transport (Rogers 2006) and its accuracy has been extensively validated in the scientific community. However, MCS is also notoriously time-consuming (Haynor *et al* 1990, Gieles *et al* 2002, De Beenhouwer *et al* 2007).

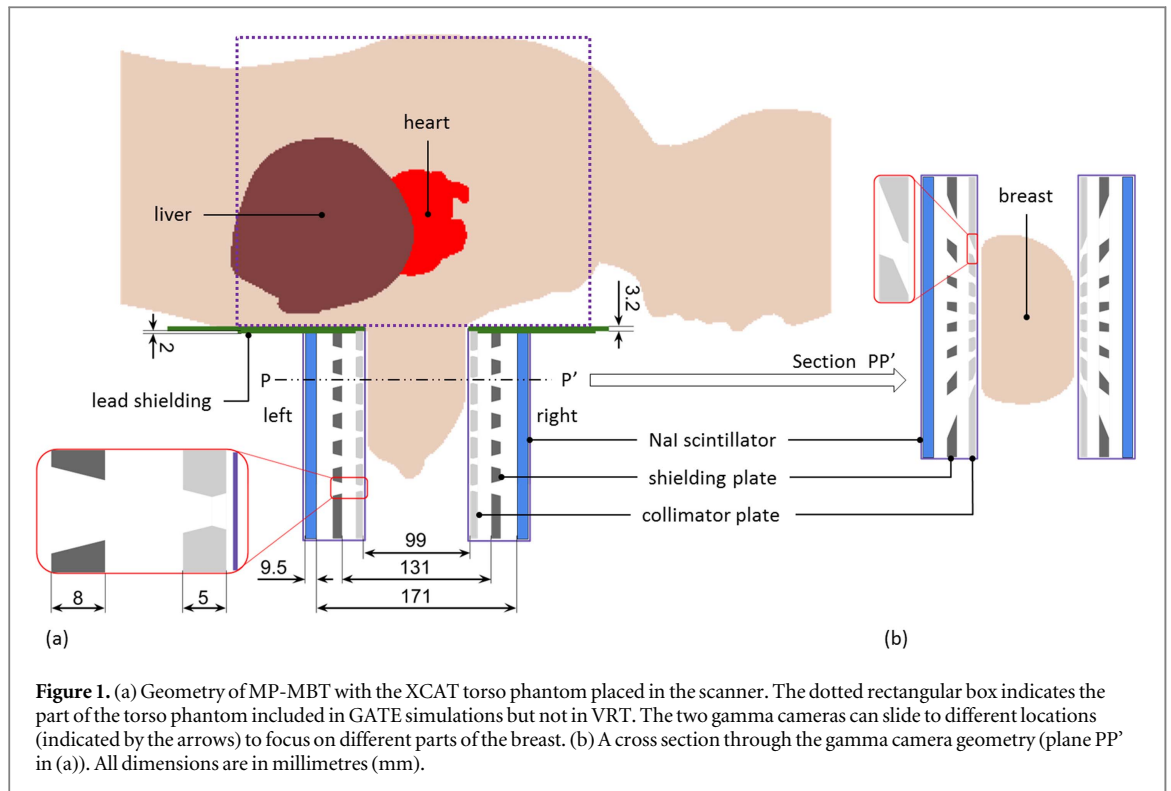
Several ways to speed up MCS exist, such as applying a large production threshold for secondary particles (Jan *et al* 2004, 2011), ignoring some of the physics processes generating secondary particles (Devries *et al* 1990, Cot *et al* 2002, 2004) or optimizing the code for a specific application (Hunter *et al* 2013). New implementation strategies based on graphics processing units (GPUs) have also recently become available (Lippuner and Elbakri 2011, Bert *et al* 2013, Garcia *et al* 2016). Another class of accelerated MCS uses variance reduction techniques such as forced detection, angular response function modeling or fictitious interaction (Haynor *et al* 1990, Wang *et al* 1993, Beekman *et al* 1999, de Jong *et al* 2001, Gieles *et al* 2002, Ljungberg *et al* 2005, Rehfeld *et al* 2009, Descourt *et al* 2010, El Bitar *et al* 2011). However, even with modern hardware and advanced acceleration techniques, for certain applications, MSC is still prohibitively slow and complete system simulations often take days (El Bitar *et al* 2011, Garcia *et al* 2016).

If the effects of scatter are negligible or correctable in a gamma imaging system, a simulation that only models attenuation but ignores scatter is a possible way to reduce the calculation time. This can be done using a simple raytracing algorithm, in which the paths from the gamma source to the detector are tracked and attenuation of gamma photons along these paths is calculated. Analytical raytracing software, in which phantom, collimator and detector geometries are described by analytical functions, has been used to generate PSFs for simple imaging systems quickly and noiselessly (Feng *et al* 2010, Goorden *et al*

2011, Li and Furenlid 2014). For complicated geometries which are difficult to describe analytically, such as irregular phantoms in CT and SPECT, discrete raytracing, in which geometries are represented by a finite number of voxels or layers, is more practical (Siddon 1985, Smith *et al* 1997, Goertzen *et al* 2002, Schramm *et al* 2003, Tabary *et al* 2004, Funk *et al* 2006, Lin *et al* 2010). Among these discrete raytracers, those that use a representation of volumes in cubic voxels (voxelized ray tracing, VRT) are the most straightforward and suitable to represent highly irregular structures.

Voxelization of continuous structures introduces simulation errors since the edges are no longer smooth but composed of cubic elements. The use of very fine voxels can reduce the error but puts a strain on memory requirements and slows down the computation time. Solutions that have been proposed to circumvent the issue of balancing accuracy and simulation time in volume representation include using hybrid analytical-voxelized representations (Wang *et al* 1993), employing non-cubic voxel shapes (Matej and Lewitt 1996, Zbijewski and Beekman 2006) or using a spatial subdivision method such as an octree voxel size structure (Meagher 1982, Glassner 1984). Octree is a method for describing an object by repeatedly dividing a cubic voxel into eight smaller cubic regions until each region becomes homogeneous. It has been applied in medical imaging simulations (Ogawa and Maeda 1995, Suganuma and Ogawa 2000, Hubert-Tremblay *et al* 2006, Sarrut and Guigues 2008, Badal *et al* 2009) and is nowadays widely used in 3D graphics for representing irregular volumes.

In previous medical imaging instrumentation research in which VRT was applied, only phantoms or detectors were represented by voxels (Siddon 1985, Smith *et al* 1997, Huesman *et al* 2000, Goertzen *et al* 2002, Schramm *et al* 2003, Tabary *et al* 2004, Lin *et al* 2010). In contrast, we developed VRT software in which all volumes (gamma emitter, phantom, collimator and gamma detector) are voxelized. Fixed voxel sizes are used in phantoms and detectors, but in the collimator volume for which precise geometrical knowledge is crucial and through which raytracing is most time-consuming, a form of an octree-like voxel structure with two different voxel sizes is used. Though VRT provides an attractive alternative to MCS in testing system geometries such as MP-MBT, its validity lies in the prerequisite that scatter is negligible or correctable. As tracer uptake in breast imaging is relatively high in organs such as the liver and heart (Wackers *et al* 1989, Maublant *et al* 1996), a careful assessment of its contribution in our MP-MBT system is required. For other breast gamma imaging geometries, different amounts of scatter contamination were reported and it is thus not *a priori* clear what the amount of scatter is in MP-MBT (Pani *et al* 1998, Gruber *et al* 1999, Williams *et al* 2003, Brzymialkiewicz *et al* 2005, Hruska and O'Connor 2006, 2008a, Campbell and Peterson 2014).



The aim of this paper is to propose our specific VRT implementation and to validate the use of VRT for MP-MBT. To this end VRT is compared against the MCS software package GATE (Geant4 Application in Tomographic Emission (Jan *et al* 2004, 2011)) which is considered to be the gold standard. PSFs, projections, and reconstructed images of the anthropomorphic XCAT phantom (Segars and Tsui 2009) are generated by both software packages, and simulation accuracy of VRT and its dependence on collimator volume voxel size settings are analysed.

2. Method

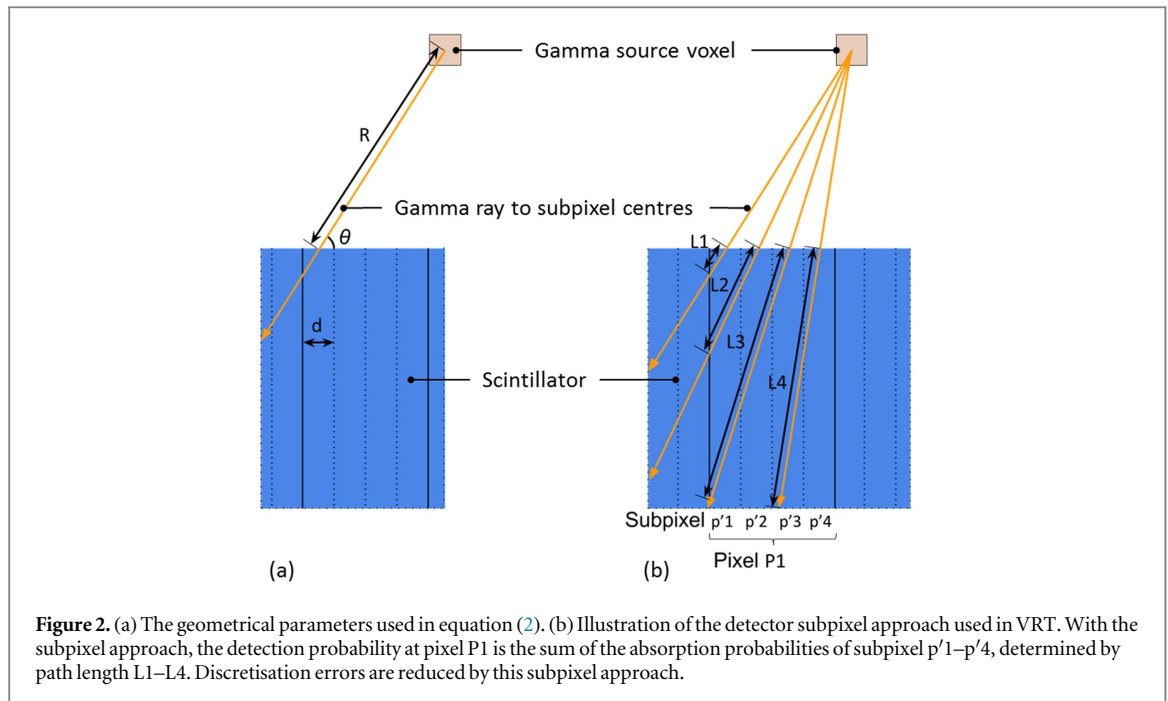
2.1. MP-MBT

The novel MP-MBT concept (shown in figure 1) was proposed in Beekman (2011) and van Roosmalen *et al* (2016) in which a detailed description can be found. MP-MBT aims to image the distribution of single-gamma emitting tracers in the breast to detect possible malignancies. The breast is pendant through a hole in the patient bed (equipped with 3.2 mm thick lead for shielding) and is mildly compressed at levels similar to planar molecular breast imaging (Hruska *et al* 2008c) with optically transparent plates, through which optical cameras (not shown in figure 1) view the breast. These optical cameras generate images, from which users can select a volume-of-interest which is to be imaged. Imaging takes place by the two gamma cameras located underneath the patient bed, each equipped with a multi-pinhole collimator focusing on a

volume smaller than the whole breast, cf figure 1(b). The gamma cameras slide to various positions during scanning in order to cover the region designated by the user. Each of the 5 mm thick collimator plates, made of tungsten alloy (97% tungsten, 1.5% nickel, and 1.5% iron), has 42 round knife-edge pinholes. An 8 mm-thick shielding plate made of the same material is located between gamma detector and collimator plate. It has 42 rectangular holes, each of them corresponding to one of the pinholes in the collimator respectively avoiding different pinhole projections from overlapping on the gamma detectors. Gamma detectors are assumed to consist of $250 \times 150 \times 9.5 \text{ mm}^3$ NaI(Tl) crystals read out by a PMT array. For 140 keV gamma photons (from $^{99\text{m}}\text{Tc}$ -Sestamibi, the most prominent tracer for breast tumour detection), 90% detection efficiency can be achieved by NaI of this thickness. With the projections obtained from the two gamma cameras, the 3D tracer distribution in the breast can be reconstructed using a maximum likelihood expectation maximization algorithm (Vastenhouw and Beekman 2007, van Roosmalen *et al* 2016).

2.2. VRT

VRT uses voxelized models of the detectors, collimators, phantoms, and the distribution of single-gamma emitters as its input. Each voxel is assigned a value which corresponds to the linear attenuation coefficient μ of its material at the energy of the gamma-emitter. When a gamma photon path crosses a voxel,



the path length L through this voxel is obtained. Siddon's raytracing algorithm is used to quickly calculate path lengths in voxels (Siddon 1985). Lambert–Beer's law,

$$P = e^{-\mu L}, \quad (1)$$

is then used to calculate the transmission probability P through the voxel. During raytracing, the transmission probabilities in the voxels that the ray passes are multiplied giving a total transmission probability. As there is always a finite probability for a gamma photon to pass through phantom and collimator, one could in principle calculate the full transmission probability along every simulated gamma ray path. However, many gamma rays pass through large amounts of collimator material (tungsten alloy), making the transmission probability extremely small and it is computationally inefficient to keep track of all these paths. We, therefore, set a cut-off of 10^{-5} (2.76 mm collimator material) on the transmission probability through phantom and collimator below which ray tracing is stopped.

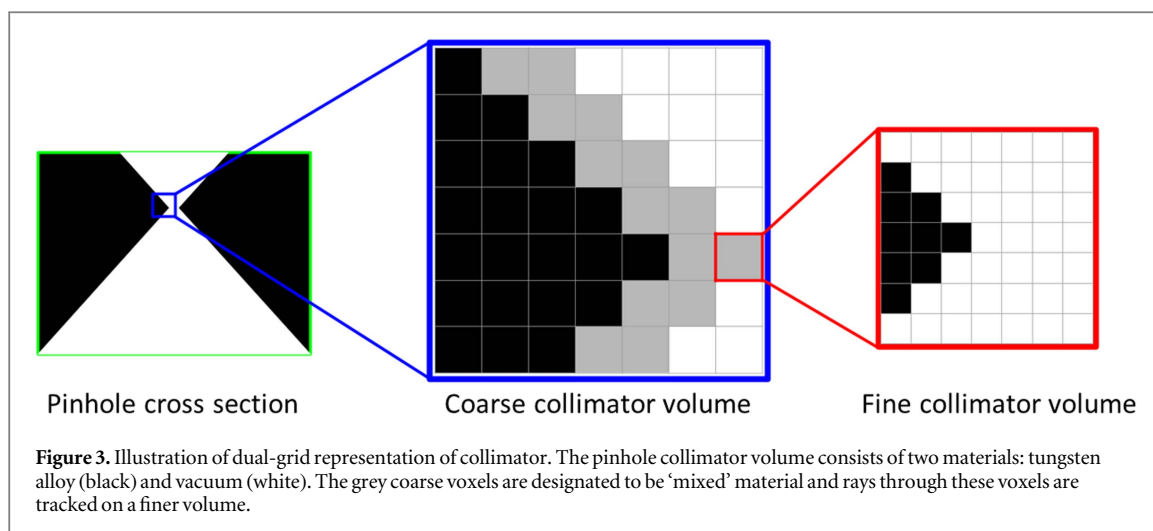
The surface of the gamma detector is divided into detector pixels and each pixel is subdivided into 4×4 subpixels. For projection image assessment the pixel size is set to 1 mm, while for PSF assessment 0.5 mm is used. Gamma photons from each source position are tracked to the centres of all subpixels. The solid angle of each subpixel is taken into account by multiplying the transmission probability through the collimator of the gamma photons by the geometrical factor

$$P_{\text{geometry}} = \frac{d^2 \sin \theta}{4\pi R^2}, \quad (2)$$

where R is the distance from the voxel centre to the detector subpixel centre, d is the detector subpixel

size, and θ is the angle of incidence of the gamma photon (see figure 2(a)).

The gamma photon is subsequently tracked through the continuous NaI(Tl) gamma detector which is represented in a voxelized form as well: it is subdivided into rectangular voxels with the length of each voxel being equal to the detector crystal's thickness (9.5 mm) and the area having the size of a detector subpixel. In the gamma detector, Lambert–Beer's law is again used to calculate the absorption probability in each detector voxel. Note that gamma photons that reach the detector under an angle can pass different rectangular voxels and this way the varying depth-of-interaction in the detector is simulated (see figure 2(b)). The attenuation coefficient of the detector is set to 0.217 mm^{-1} . This number is higher than the attenuation coefficient that solely includes photoelectric effect but lower than the total attenuation coefficient for 140 keV gammas in NaI (including Compton scatter). In fact, we set the attenuation coefficient such that the number of detected gammas in VRT with this attenuation coefficient is equal to the number of detected gammas found in the $\pm 10\%$ photopeak from GATE simulated PSFs. Thus, the added detector efficiency due to gamma photons undergoing multiple interactions in the scintillator is accounted for in VRT, but the scatter process itself, which may impact spatial resolution, is not taken into account. Finally, for each source position, absorption probabilities in all 4×4 detector subpixels corresponding to a detector pixel are added. The detector projection image acquired is then blurred with a Gaussian filter with 3.2 mm FWHM in order to simulate the intrinsic detector resolution. The idea of subdividing detector pixels to enhance modelling accuracy has been successfully applied in Huesman *et al* (2000) and Lin *et al*



(2010) and the usefulness of this approach in MP-MBT will be evaluated in the results section.

The voxel sizes of collimator and shielding plates can have a significant impact on simulation results and they thus have to be chosen carefully. Generally, a small voxel size is preferable because it allows one to better approximate the continuous structures in the geometry, but it also puts a strain on memory requirements and simulation time. To circumvent this issue, a dual-grid approach is used based on the idea of octree structure (Glassner 1984, Badal *et al* 2009). Figure 3 is a 2D illustration of this approach: two different voxel sizes, a coarse one and a fine one, are used for the collimator/shielding volume. Initially, a photon is traced through the coarse voxel volume. In the coarse voxel volume, each voxel is designated to have one particular linear attenuation coefficient or it is assumed to be 'mixed' (i.e. the coarse voxel contains fine voxels with different linear attenuation coefficients). When a gamma ray is tracked through the coarse voxels, cumulative attenuation in the non-'mixed' voxels is calculated. When the ray reaches a 'mixed' voxel, VRT looks for the fine grid of this coarse voxel and continues raytracing in the fine voxels until the ray exits this coarse voxel. VRT checks whether the probability of transmission is lower than the cut-off after every fine/coarse voxel tracing.

With this dual-grid raytracing approach, the voxel size of the fine volume determines the accuracy of simulation while the combination of fine and coarse voxel sizes sets the computational speed. In this paper we first test six fine voxel sizes (1/2 mm, 1/4 mm, 1/8 mm, 1/16 mm, 1/32 mm, 1/40 mm) to determine the accuracy that we can achieve (with coarse voxel size fixed at 1 mm). Then, in order to optimize speed, we check six coarse voxel sizes (1/4 mm, 1/2 mm, 1 mm, 2 mm, 3 mm, 5 mm) to find out which one allows for the highest speed (with the optimal fine voxel size found above).

2.3. MCS

To validate VRT, we use the MCS package GATE (Jan *et al* 2004, 2011), which is well-validated in gamma-ray imaging, radiation therapy, x-ray imaging, and optical imaging (Assie *et al* 2005, Lamare *et al* 2006, Schmidlein *et al* 2006, Staelens *et al* 2006, Brunner *et al* 2009, Chen *et al* 2009, van der Laan *et al* 2010, Grevillot *et al* 2011). GATE 7.0 with Geant4 9.6 running on a CentOS 6.6 cluster is used. Only the photoelectric effect, Compton scattering, and Rayleigh scattering are included in the physics list, since other physics processes are not expected to play major roles in our application (Devries *et al* 1990, Cot *et al* 2002, 2004). The same geometry as simulated with VRT is also built in GATE. As we aim to assess the influence of finite voxel size in VRT, the collimator and shielding plates are generated with analytical shapes (head-to-head cones, trapezoids, and boxes), such that the GATE simulation does not suffer from discretisation effects due to the finite voxel size. The *adder digitizer* is applied to GATE outputs, which automatically records the interaction time, deposited energy, and energy-weighted averaged scintillator interaction position (Jan *et al* 2004). Gaussian blurring of energy is applied to each detector pixel to achieve 9% FWHM energy resolution, and Gaussian blurring in the spatial domain is also applied to simulate 3.2 mm FWHM resolution (as is done in VRT). To note, the blurring in energy and spatial domain acts as an acceleration factor of MCS and reduces noise. As we aim to compare GATE simulations with noiseless VRT, such a noise reduction is desirable. A difference between GATE photon tracking and VRT is that in GATE the gamma photons can be emitted in any possible direction, while in VRT only gamma photon paths from the centres of the gamma source voxels to the centres of the detector subpixels are accounted for. Figure 4 shows one of the two gamma cameras in GATE.

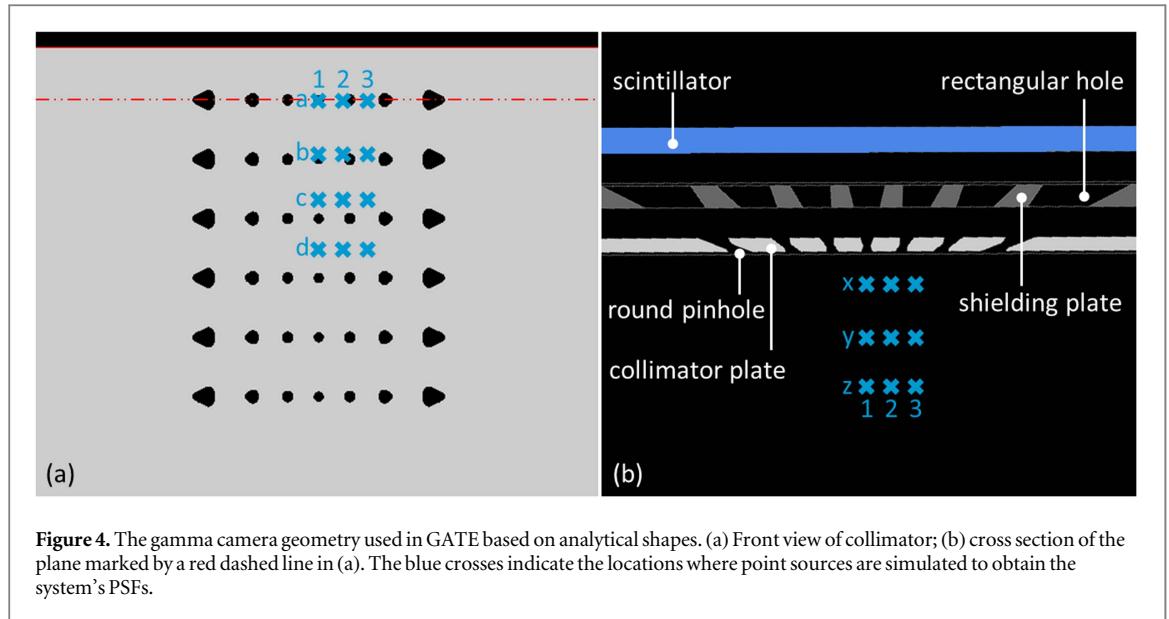


Figure 4. The gamma camera geometry used in GATE based on analytical shapes. (a) Front view of collimator; (b) cross section of the plane marked by a red dashed line in (a). The blue crosses indicate the locations where point sources are simulated to obtain the system's PSFs.

2.4. VRT accuracy and fine voxel size optimisation

To study the accuracy of VRT for different voxel sizes (of the fine volume), PSFs are obtained with VRT and GATE from point sources (ideal point source of infinitely small size) placed in the vacuum at 36 locations in front of the gamma camera (the blue crosses in figure 4). The position designated by ax1 is 11.5 mm from the front surface of the collimator plate and right on the axis of the central pinhole. The vertical interval (e.g. a–b distance) between these locations is 20 mm, the horizontal interval (e.g. 1–2 distance) is 10 mm, and the depth interval (e.g. x–y distance) is 20 mm. These 36 positions cover about a quarter of the field of view and are representative of the whole field of view due to the symmetric allocation of the pinholes. Therefore, the voxel sizes optimised for these PSFs should also be the optimal voxel sizes for calculating the whole system matrix (containing all PSFs). To find how the fine voxel size influences accuracy, a sufficiently long GATE simulation of 5×10^{10} isotropic emissions is done to obtain an almost noiseless reference PSF at each source location. The normalised root-mean-square error (NRMSE) between the PSFs obtained by VRT simulations with different fine voxel sizes (see section 2.2) and the reference PSFs is calculated. It is defined by

$$\text{NRMSE}_{\text{GATE,VRT}} = \frac{\sqrt{\sum_{x=1}^X \sum_{y=1}^Y (n_{\text{GATE}}(x, y) - n_{\text{VRT}}(x, y))^2}}{XY} \cdot \frac{1}{n_{\text{GATE,max}} - n_{\text{GATE,min}}}, \quad (3)$$

where x and y are detector pixel indices. There are $X \times Y$ pixels in the PSF image and $n_{\text{GATE}}(x, y)$ and $n_{\text{VRT}}(x, y)$ are the number of counts in detector pixel (x, y) obtained with GATE and VRT respectively. $n_{\text{GATE,max}} - n_{\text{GATE,min}}$ is the range of counts in the

PSF obtained by GATE. The average NRMSE over PSFs from all 36 positions (referred to as a PSF-set) is calculated for each of the fine voxel sizes tested for VRT. In this comparison, the voxel size of the coarse volume, which does not influence simulation accuracy but only affects simulation time, is fixed to be 1 mm. The detector pixel size is fixed at 0.5 mm for all PSF simulations.

2.5. VRT time-efficiency and coarse voxel size optimisation

To optimize the time-efficiency of VRT, the same PSFs as described in section 2.4 are again simulated with the optimized fine voxel size for six different VRT coarse voxel sizes (see section 2.2) and the simulation times are recorded. This way the coarse voxel size which resulted in the fastest simulation could be determined.

Subsequently, we compare the time-efficiency of VRT with optimized voxel settings to that of GATE. For a comparison, one has to choose a setting for the number of photons tracked in GATE. For the validation study, we track 5×10^{10} photons at each point source position as this results in almost noiseless PSFs and can thus serve as a gold standard. If fewer photons are tracked, PSFs become noisier and thus start to deviate from the gold standard. Although this deviation from the gold standard is due to different reasons than the deviation obtained with VRT (which can be due to neglect of physics processes, scatter, or discretisation effects) we choose to determine the relative time-efficiency of VRT compared to GATE, by comparing the time it takes for GATE to arrive at the same difference level from the gold standard as VRT (again characterized by NRMSE). To this end, PSF-sets from GATE simulations with a series of different numbers of emissions are generated and NRMSE from the gold standard is calculated for each of them. Moreover, as is mentioned in section 2.3, GATE simulation results are

Table 1. Tracer uptake in different tissues.

Tissue	Uptake
Breast	3.7 kBq ml ⁻¹
Torso	3.7 kBq ml ⁻¹
Heart	55.5 kBq ml ⁻¹
Liver	55.5 kBq ml ⁻¹

blurred in energy and spatial domain with Gaussian kernels in order to mimic the desired energy and spatial resolution. The use of a kernel-based way of simulating resolution instead of picking a random detector position and energy value from the detector response function (a full MCS) is a way of accelerating MCS and it is very useful in case one is interested in noiseless PSFs. Throughout this paper, we use accelerated MCS to avoid too lengthy simulations, but in the time-efficiency comparison, we also provide acceleration factors of VRT with respect to full MCS, in which the interaction energy and position are, instead of blurred, randomised according to a 9%-FWHM and 3.2 mm-FWHM Gaussian distribution respectively. In our time comparison study, all simulations are executed on the same multi-CPU computer cluster, and 25 CPUs are used.

2.6. Projection image comparison

In MP-MBT, the scattered gamma photons from torso and breast can be detected by the gamma detector and if the energy of these scattered photons is within the photopeak window, they will usually add a rather continuous background to the projection image. As tracer uptake in organs is rather high in breast imaging, scatter is a topic of concern in molecular breast imaging and in some designs high energy resolution gamma detectors are used (Mueller *et al* 2003, Hruska *et al* 2012a, Hruska *et al* 2012b). The amount of scatter that will be detected depends on the exact system geometry and different studies have reported very different numbers (Pani *et al* 1998, Gruber *et al* 1999, Williams *et al* 2003, Brzymialkiewicz *et al* 2005, Hruska and O'Connor 2006, 2008a, Campbell and Peterson 2014).

It is thus important to evaluate the influence of scatter in MP-MBT with a realistic anthropomorphic phantom. For this reason, we implement the well-known XCAT phantom with heart, liver, torso, and deformable breasts in the GATE simulation, see figure 1 (Li *et al* 2009, Segars and Tsui 2009, Segars *et al* 2010). Instead of using dual-grid voxels, the voxel sizes of the XCAT phantom are fixed: the torso, including the heart and the liver, is voxelized to a 3.2 mm grid, and the breast is voxelized to a 0.8 mm grid. Two breast sizes are checked: a 400 ml breast compressed to a thickness of 55 mm (a common B-cup breast), and a 1300 ml breast compressed to a thickness of 85 mm (a common D-cup breast). The

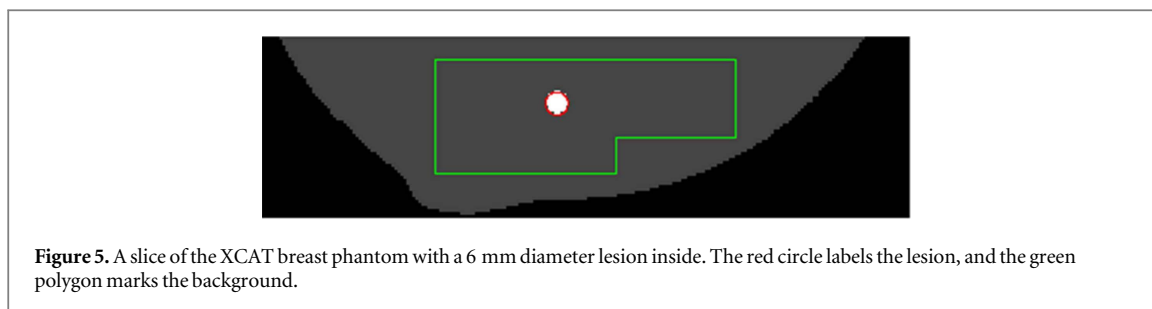
latter breast is shown in figure 1. To note, the distance between the two collimators is larger than the thickness of the breast because of the 7 mm thick compression plate. The tracer uptake that we assumed in different organs is listed in table 1. These are typical numbers found in practice if 925 MBq ^{99m}Tc-Sestamibi is injected to the patient (Wackers *et al* 1989, Maublant *et al* 1996, Wang *et al* 1997, Brzymialkiewicz *et al* 2005, Hruska and O'Connor 2008a, 2008b, Perez *et al* 2010).

In GATE, the detected photons are categorised according to their origin and interactions they have undergone: they are listed to be either breast-emitted or torso-emitted, and scattered or non-scattered. This way we are able to divide the total energy spectrum into different categories in order to better pinpoint which photons cause possible differences with VRT. Moreover, we apply the widely acknowledged triple-energy window (TEW) scatter correction method to GATE simulated projections, in order to check if the scatter can be estimated this way (Ogawa *et al* 1991). We set a $\pm 10\%$ photopeak window (126–154 keV), a 14 keV wide left side window (119–133 keV), and a 14 keV wide right side window (148–161 keV). For a certain detector pixel with N_L counts in the left side window and N_R counts in the right side window, scatter is then estimated to be

$$N_S = \frac{N_L + N_R}{2} \times \frac{28 \text{ keV}}{14 \text{ keV}} \times 0.6. \quad (4)$$

To note there is a factor 0.6 in (4), which aims to make the total counts after TEW correction the same as acquired with VRT. In reality, when the number of scattered photons is not known one may base this number either on simulations or different values may be tested in an optimization study. We subtract this scatter estimate from the simulated projections to obtain TEW-corrected projections. The occurrence of negative values in the projections is prevented by setting them to zero. Note that the comparison of VRT images with scatter-corrected GATE images is relevant to assess bias as in real scanners a TEW-based scatter correction method is commonly applied.

Full projection images (with scatter), scatter-free GATE projections, TEW-corrected GATE projections, and VRT projections of the same phantom scan are compared. To note, in the VRT simulations, only the compressed breast phantom is included while the torso phantom is neglected. Additionally, in generating projections, VRT only tracks the rays through the breast phantom (single grid). The subsequent raytracing through the collimator (dual-grid) is done using previously acquired PSFs that were stored on disk. The transmission probability obtained from raytracing through the phantom is then multiplied by the corresponding collimator raytracing transmission factor. This gives exactly the same results as a complete raytracing simulation from each activity containing



voxel in the phantom through the collimator to the detector but is more efficient.

2.7. Image reconstruction

The comparison of PSFs and projection images allows one to estimate how accurate VRT is in the noiseless case and to what extent the TEW method corrects for the bias caused by scattered photons. However, when simulating reconstructed images with realistic noise levels, neglecting scatter may also lead to an underestimation of noise in images as detector images of scattered photons are noisy themselves. To better investigate the impact of this, we also simulated a full scan of the 400 ml breast phantom with a 6.0 mm diameter spherical lesion inside (see figure 5) using both GATE and VRT to obtain projection images. For normal breast tissue and organs we assume the realistic activity levels provided in table 1 while the lesion uptake is taken to be 37 kBq ml^{-1} , ten times as high in normal breast tissue. The total scan time is assumed to be 10 min. In case GATE is used to simulate projection images, the number of gamma emissions corresponding to the given activity levels and scan time are simulated. When VRT is used, noiseless projection images are generated (similar as described in section 2.6) after which Poisson noise is applied. In order to be able to acquire 3D reconstructions, projection images are acquired for a total of 170 different positions of the sliding gamma detectors. Precise information on the positions used and other scan details can be found in van Roosmalen *et al* (2016).

The projections generated by either GATE or VRT are used as the input of a maximum likelihood estimation maximisation (MLEM) reconstruction algorithm, while the system matrix used in MLEM in both cases is generated by VRT. Data acquired from different gamma detector positions are all simultaneously taken into account in image reconstruction (Vastenhouw and Beekman 2007). In case GATE-generated projections are used, TEW scatter correction is applied to compensate for scatter from the breast and torso. In that case, scatter images are obtained in the same way as in section 2.6 but an additional Gaussian filter with 11.8 mm FWHM is applied to smooth them. The

reason to blur the scatter images is to limit the noise amplification due to TEW correction as is usually done (Ichihara *et al* 1993, Hashimoto *et al* 1997). The scatter images are then added to the simulated projections in the denominator of the MLEM algorithm similar as summarised in Hutton *et al* (2011). Note that the size of the smoothing filter and the side windows chosen are not optimised in this study. While voxel size of the phantom in VRT and GATE simulations was set to 0.8 mm, voxel size of reconstructed images was 1.6 mm, in order to mimic a realistic continuous activity distribution.

Ten GATE simulations and ten noise realisations of VRT-simulated projections are used to generate reconstructed images. Besides visually comparing reconstructed images, we also compared the mean contrast of the lesion over the background, as well as the noise as standard deviation in the background. Figure 5 shows how we defined the regions used; the area inside the 6 mm diameter red circle is considered to be lesion area, while the area $>3 \text{ mm}$ outside the red circle but still inside the green polygon is considered to be background area.

3. Results

3.1. VRT accuracy for generating PSFs

In figure 6, an example PSF profile is shown for collimators parametrized by different fine volume voxel sizes. From this image, one can see that the setting of the fine voxel size influences the accuracy of generating PSFs, especially near the PSF maximum. The counts of the GATE-generated PSF (considered to be the ground truth) are normalised to the total number of emissions of the point source (5×10^{10}) so that the total counts in a PSF represent the sensitivity of the scanner. No scaling factor needs to be applied to VRT-generated PSFs as a solid angle is taken into account. As explained in section 2, photons that scatter in the collimator or scintillator and end up being detected in the photopeak are included in GATE-generated PSFs.

In table 2, the differences between VRT-simulated PSFs and GATE-simulated reference PSFs are quantified by means of the NRMSE, averaged over the

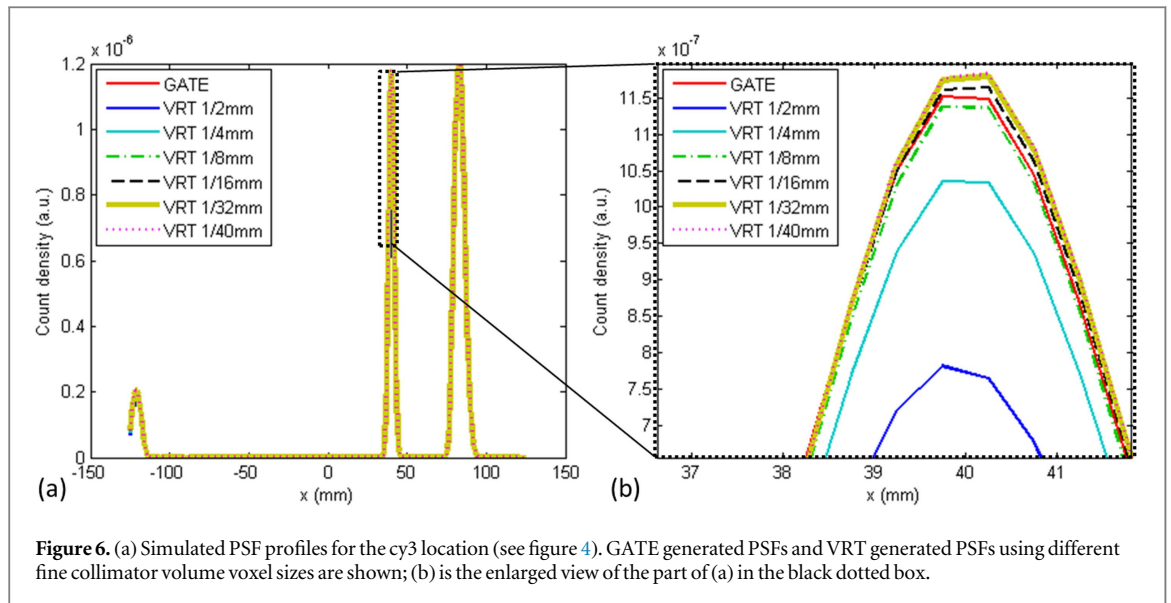


Figure 6. (a) Simulated PSF profiles for the cy3 location (see figure 4). GATE generated PSFs and VRT generated PSFs using different fine collimator volume voxel sizes are shown; (b) is the enlarged view of the part of (a) in the black dotted box.

Table 2. Comparison of simulation accuracy for different fine volume voxel sizes (coarse volume voxel fixed at 1 mm).

Fine volume voxel size	Diff. from reference	
	NRMSE	Max. diff.
1/2 mm	0.601%	33.13%
1/4 mm	0.234%	11.21%
1/8 mm	0.143%	5.07%
1/16 mm	0.140%	5.32%
1/32 mm	0.150%	6.34%
1/40 mm	0.151%	6.18%

36 point source positions. The maximum difference over the 36 positions is also provided. From the table, we can infer that the differences between VRT and reference PSFs become smaller when the fine volume voxel size is decreased from 1/2 mm to 1/8 mm. Therefore we choose 1/8 mm to be the fine voxel size in subsequent simulations. For smaller voxel sizes the error does not decrease anymore and even slightly increases. This slight unexpected increase will be discussed later. In the current VRT simulation, every detector pixel is divided into 4×4 subpixels in the simulation. Without this subpixel approach, the NRMSE and maximum difference for the 1/8 mm fine voxel size increase to 0.230% and 11.83% respectively. Therefore, the subpixel approach does improve the accuracy of VRT and is also applied in the subsequent comparison.

Figure 7 shows several PSFs at different locations in the field of view obtained with GATE (reference) and VRT with the 1/8 mm fine voxel size setting. The profiles are shown on both linear and semi-logarithmic scales. These profiles confirm that GATE and VRT give very similar PSFs as could also be assessed from the numbers in table 2.

It is worth noting that in the semi-log scale graphs (figures 7(b), (e), and (h)), the amplitude of VRT-generated PSFs goes to zero at locations in between pinholes while GATE-generated PSFs do not. The reason that there is zero signal for VRT is the result of the applied cut-off described in section 2.2, that results in ray-tracing being stopped when traversing more than 2.76 mm of collimator material. In GATE, such a cut-off is not applied and as scattered photons are included there can be a signal in any detector pixel. By analysing the simulation results, we found that the signal in between pinholes is mainly caused by gamma photons that undergo multiple interactions in the scintillator. In this situation, the total energy deposition can still be within the $\pm 10\%$ photopeak meaning that these photons are included, and the interaction position is estimated at the centroid of different interaction positions. Note that the signal in between pinholes is extremely small showing that all though VRT only includes detector scatter by adapting the NaI attenuation coefficient, it is well able to simulate MP-MBT including resolution degradation due to multiple scatter in the scintillator.

3.2. VRT time-efficiency optimisation

While the accuracy of VRT is only determined by the fine voxel size, the time-efficiency also depends on the coarse voxel size. In table 3, the simulation time of VRT (total time required for obtaining the 36 PSFs) for different settings of the coarse volume voxel size is listed. A coarse voxel size of 2 mm is optimal in terms of computational speed and we therefore choose 2 mm as the coarse voxel size for this scanner in subsequent simulations. Table 3 also confirms that the accuracy of VRT remains the same once the fine voxel size is fixed.

To determine the relative speed of VRT compared to GATE, one has to set the number of emissions that

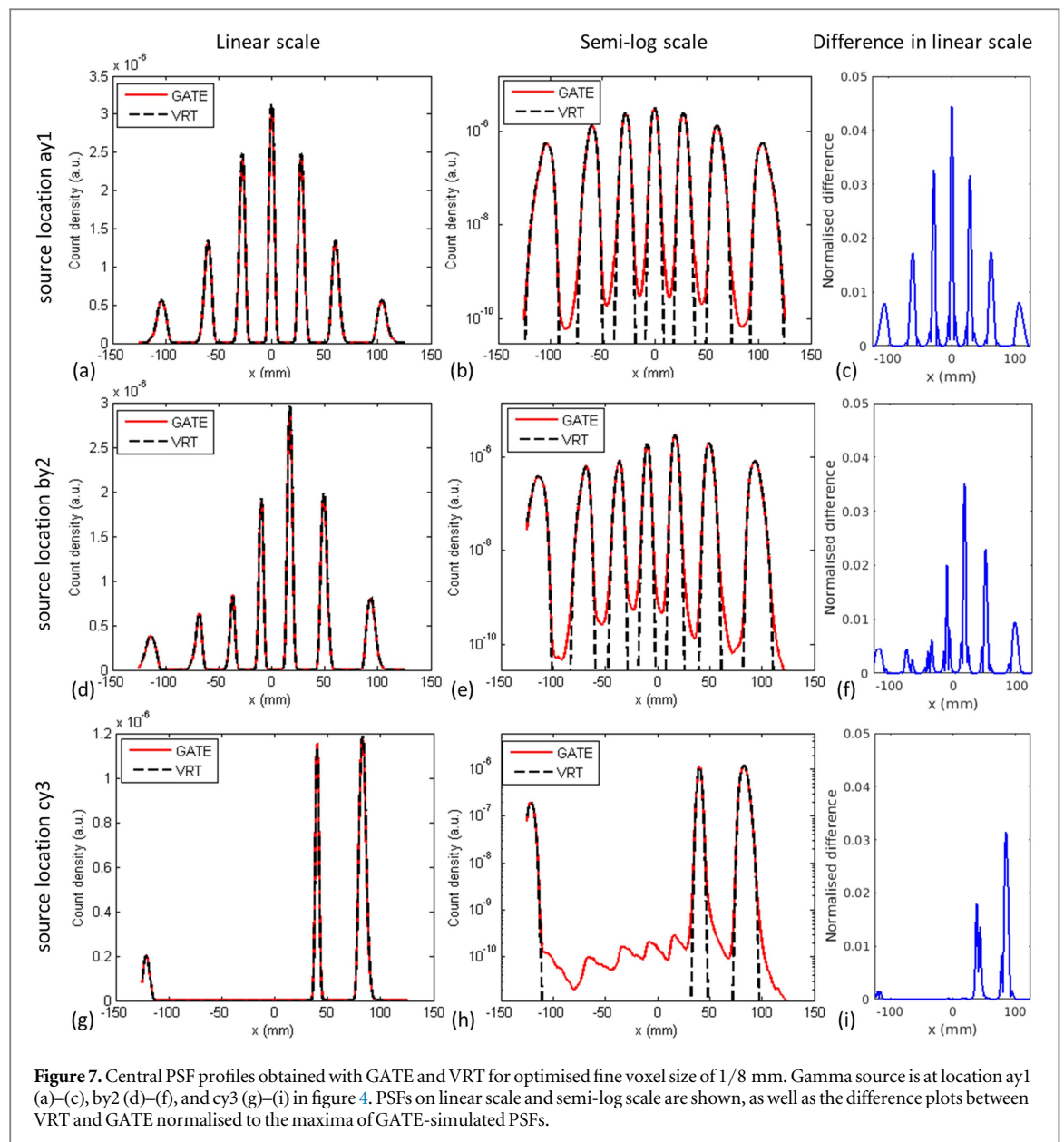


Figure 7. Central PSF profiles obtained with GATE and VRT for optimised fine voxel size of 1/8 mm. Gamma source is at location ay1 (a)–(c), by2 (d)–(f), and cy3 (g)–(i) in figure 4. PSFs on linear scale and semi-log scale are shown, as well as the difference plots between VRT and GATE normalised to the maxima of GATE-simulated PSFs.

Table 3. Comparison of different voxel sizes for the coarse volume (fine volume voxel fixes at 1/8 mm).

Coarse volume voxel size	Time in VRT	Diff. from reference
		NRMSE
1/4 mm	122 s	0.143%
1/2 mm	67 s	0.143%
1 mm	38 s	0.143%
2 mm	24 s	0.143%
3 mm	41 s	0.143%
5 mm	65 s	0.143%

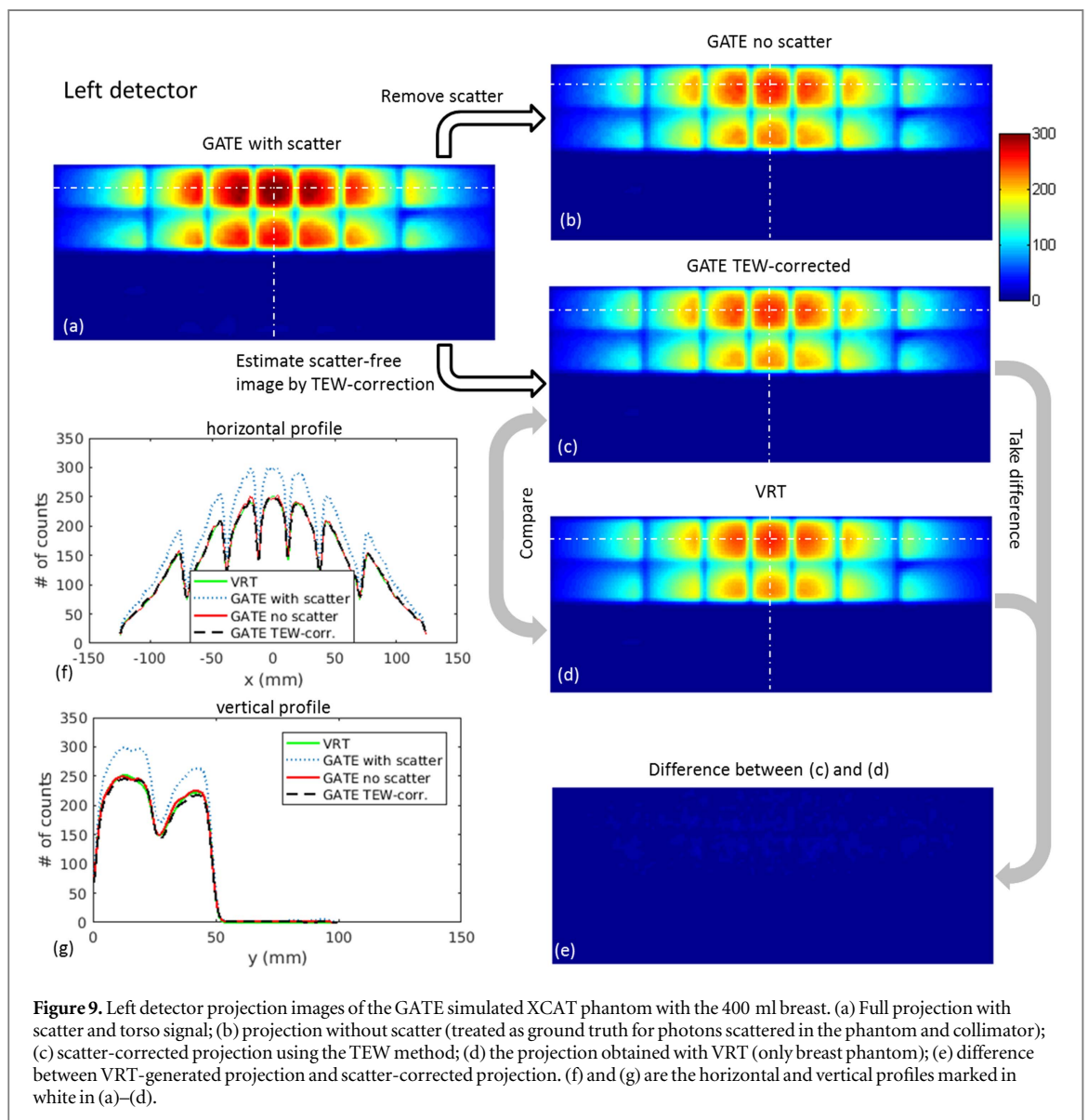
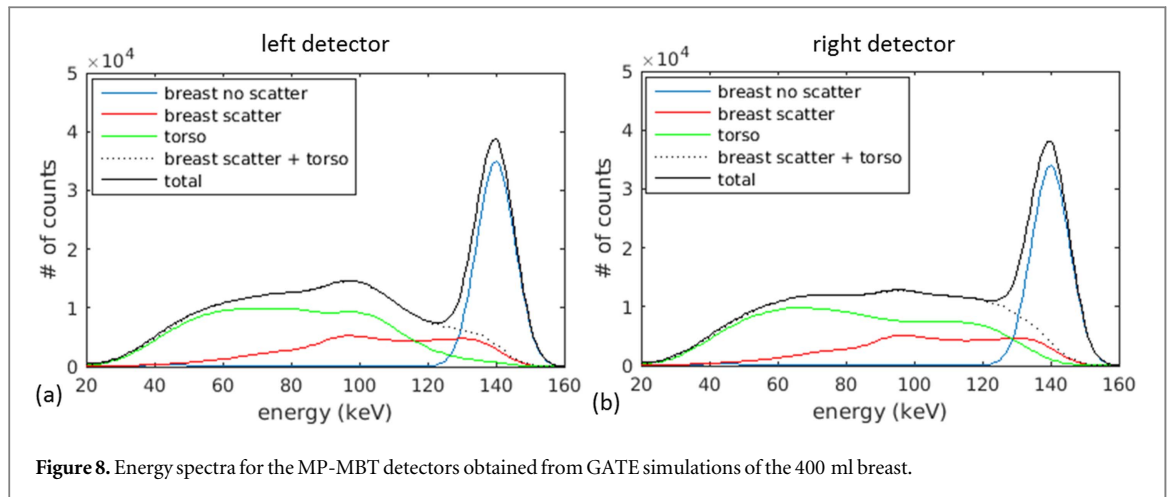
has to be simulated in GATE. If the number of emissions decreases, PSFs become noisier and there is a difference to the reference (almost) noiseless PSFs with 5×10^{10} emissions simulated. The number of

emissions that have to be simulated by accelerated (blurred) and full GATE to obtain the same difference level from the gold standard as VRT is 1.5×10^7 and 1.3×10^9 emissions respectively. For this number of emissions, VRT with optimized coarse voxel size is 337 times faster than accelerated GATE and 29 300 times faster than full GATE. However, one should note that the sources of the deviation from the reference PSF are different: in GATE deviations are caused by stochastic noise, while in VRT they are due to the minor residual mismodelling of the system.

3.3. Projection image comparison

3.3.1. Phantom representing 400 ml breast

Figure 8 shows energies of detected photons for the XCAT phantom simulation. Energy spectra are separated into different parts determined by the origin of the gamma photons ('breast' or 'torso') and the types



of interactions they undergo before being detected ('scatter' or 'no scatter'). Here 'scatter' refers to both Compton and Rayleigh scatter in the phantom and collimator, while single scatter and multiple

interactions in the scintillator are always included in all simulations. We did not distinguish between 'torso scatter' and 'torso no scatter' in the figures because the 'torso no scatter' fraction is too small to be visible in

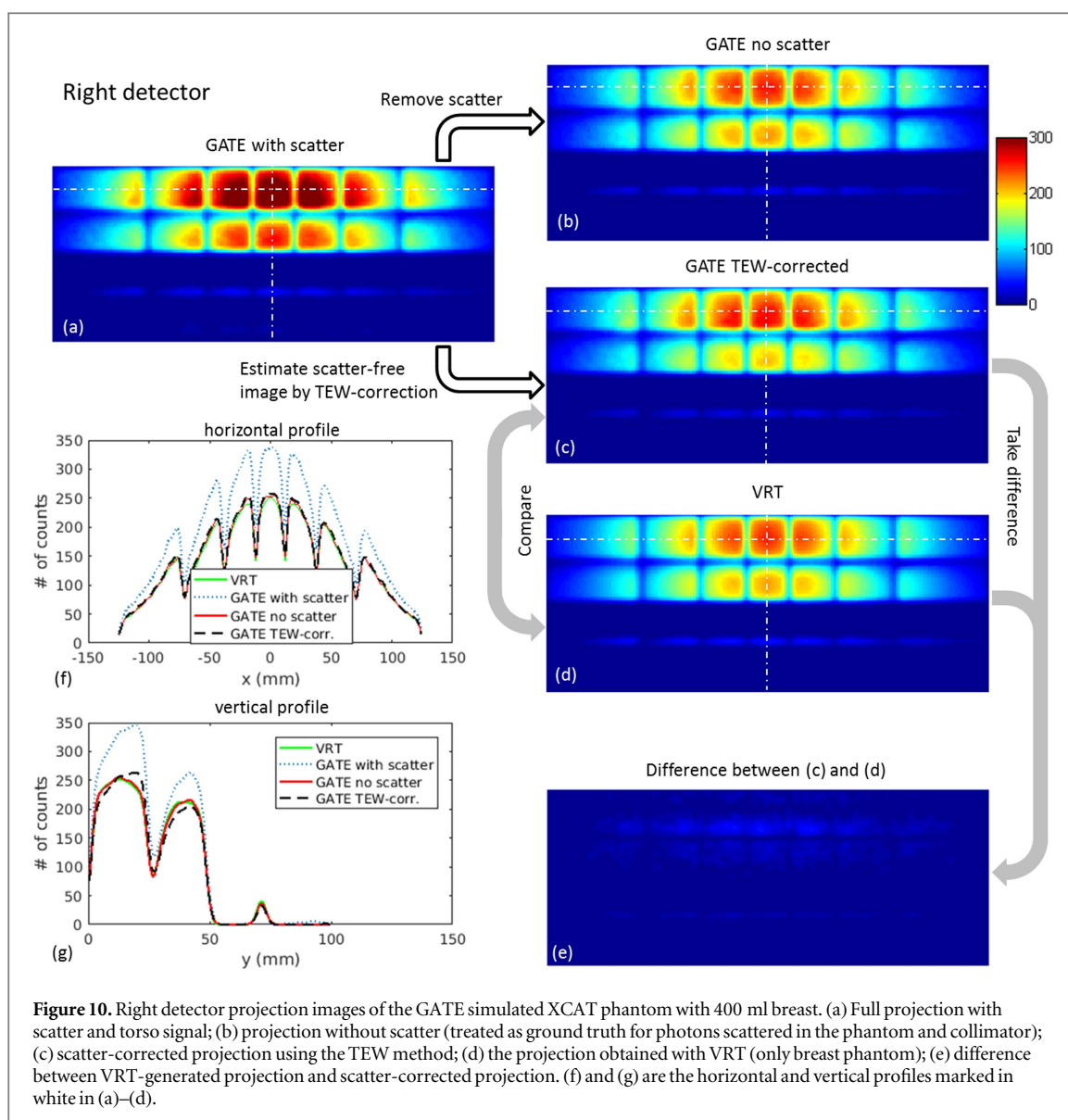


Figure 10. Right detector projection images of the GATE simulated XCAT phantom with 400 ml breast. (a) Full projection with scatter and torso signal; (b) projection without scatter (treated as ground truth for photons scattered in the phantom and collimator); (c) scatter-corrected projection using the TEW method; (d) the projection obtained with VRT (only breast phantom); (e) difference between VRT-generated projection and scatter-corrected projection. (f) and (g) are the horizontal and vertical profiles marked in white in (a)–(d).

the whole detector spectrum. Figure 8(a) corresponds to the left detector (i.e. the detector closest to the liver, see figure 1), and figure 8(b) corresponds to the right detector. The scatter fraction (the amount of gamma photons scattered in the phantom or collimator that get detected in the $\pm 10\%$ photopeak window) is about 20% on both detectors. The torso fractions (the amount of gamma photons originating from the torso) are 4% and 9% in the photopeak on the left and right detector respectively.

Projection images obtained by GATE and by VRT for the same phantom are shown in figures 9 and 10, as well as the profiles marked in white. In these images, a scatter-free projection (by simply ignoring photons that scattered in phantom and collimator) and a TEW-corrected projection are shown as well. The projection pattern from the pinholes can clearly be distinguished. These pinhole projections are non-overlapping, because of the design of the shielding plate in between

the multi-pinhole collimator and detector. Note that in these projection images only part of the detectors is used because these images are for the smaller (400 ml) breast. The projections from VRT are very similar to those from the scatter-corrected GATE projections and, as expected, scatter-free GATE projections. Since the TEW-corrected projections and the VRT-generated projections are very similar, the difference is hardly visible on the same colour scale. Therefore, we provide the same difference images shown in a different colour scale in the supplementary material, available online at stacks.iop.org/BPEX/3/045021/mmedia.

3.3.2. Phantom representing 1300 ml breast

In figure 11, the same energy spectra as in figure 8 are shown for the larger (1300 ml) breast. Corresponding projections and profiles can be found in figures 12 and 13. Like for the 400 ml breast, the scatter fraction in the

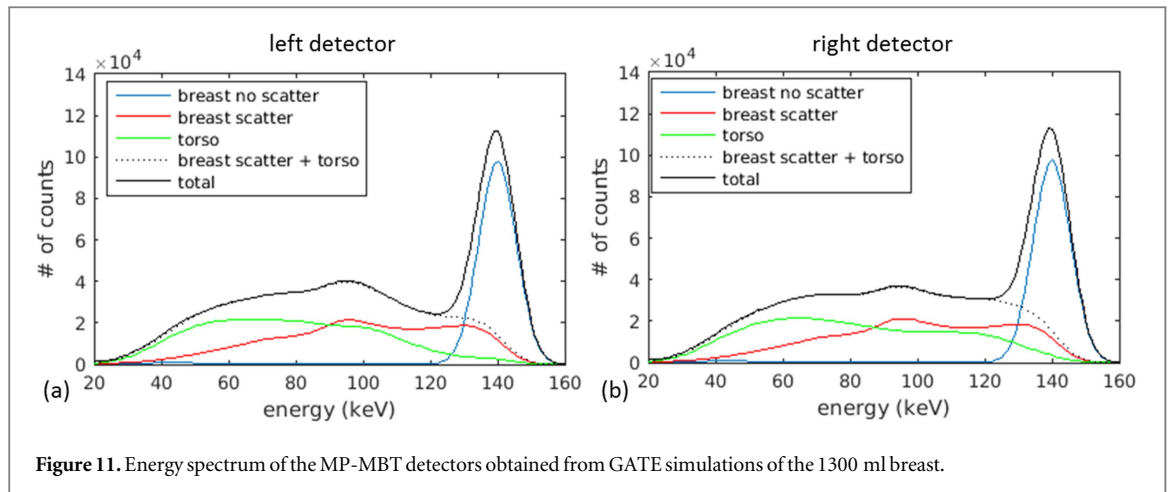


Figure 11. Energy spectrum of the MP-MBT detectors obtained from GATE simulations of the 1300 ml breast.

$\pm 10\%$ photopeak window is about 20% on both detectors. The torso fractions are 4% and 7% in the photopeak on the left and right detectors respectively.

In contrast to the projections for the smaller breast shown in figures 9 and 10, in figure 13 there is a discrepancy between the GATE projections and the projections simulated by VRT. To understand the cause of the difference, it is important to note that the TEW-corrected GATE projection is very close to the scatter-free GATE projections. Apparently, scatter can be well corrected for with the TEW method and the photons missed by VRT are not scattered photons but primary (non-scattered) photons. We will return to this issue in section 4.

In table 4, the differences between the TEW-corrected projection image and the VRT projection image are quantified in terms of NRMSE for both breast sizes. The maximum differences are listed as well. The NRMSE and maximum difference in the 1300 ml right breast are especially large, which reflects the discrepancy in figure 13.

3.4. Reconstructed images

Figure 14 shows the same slice (3.2 mm thick) through reconstructed images obtained from (a) GATE-simulated projections, and (b) VRT-generated noisy projections. TEW scatter correction is applied in case GATE-simulated projections were used. These images are post-filtered by a 3D Gaussian filter of 3 mm FWHM. Visually, reconstructions from GATE-simulated projections with TEW correction applied and from VRT-generated noisy projections appear very similar. The profiles between the two green lines in (a) and (b) are shown and compared in (c). Similar images from different noise realisations can be found in the appendix.

As noisy images cannot be directly compared as was done for noiseless projections, we also assess noise and contrast in reconstructed images for ten sets of GATE-simulated projections with TEW-

correction and ten noise realisations of VRT-simulated projections. The average contrast and noise of the lesions and backgrounds are provided in table 5, as well as the standard deviation over different noise realisations. There is no significant difference in the numbers for the different methods.

4. Discussion

From the PSF profiles in figures 6 and 7 and the differences displayed in table 2, it is clear that the PSFs from GATE and VRT (at 1/8 mm fine voxel) agree very closely. Note that initially when the fine voxel size in VRT is decreased, the PSFs acquired by GATE and VRT become more similar as one would expect. However, for voxel sizes below 1/8 mm the difference goes up slightly. From this, we conclude that for such very small voxel sizes the difference between GATE and VRT is no longer dominated by the discretisation effect and thus we deemed a fine voxel size of 1/8 mm to be sufficiently small. We do not have an exact explanation for the increasing difference between GATE and VRT for smaller voxel sizes. The small residual differences (on average 0.14%) may be caused by (i) the reference GATE simulation not being completely noiseless, or (ii) photons that scattered in collimator or detector.

Together with the 1/8 mm fine voxel size which is necessary for simulation accuracy, we find that a coarse voxel size of 2 mm led to the highest simulation speed. The optimal coarse voxel size strikes a good balance between two extremes. When it is too large, the number of mixed voxels increases and thus many more rays have to be tracked on the fine collimator grid: in the extreme situation in which the whole collimator plate is made out of a single coarse voxel, VRT will have to look into the fine volume for every photon path and the dual-grid method is actually not used. On the other hand, if the coarse voxel size is very small, raytracing on the coarse voxel grid itself is already slow and completely

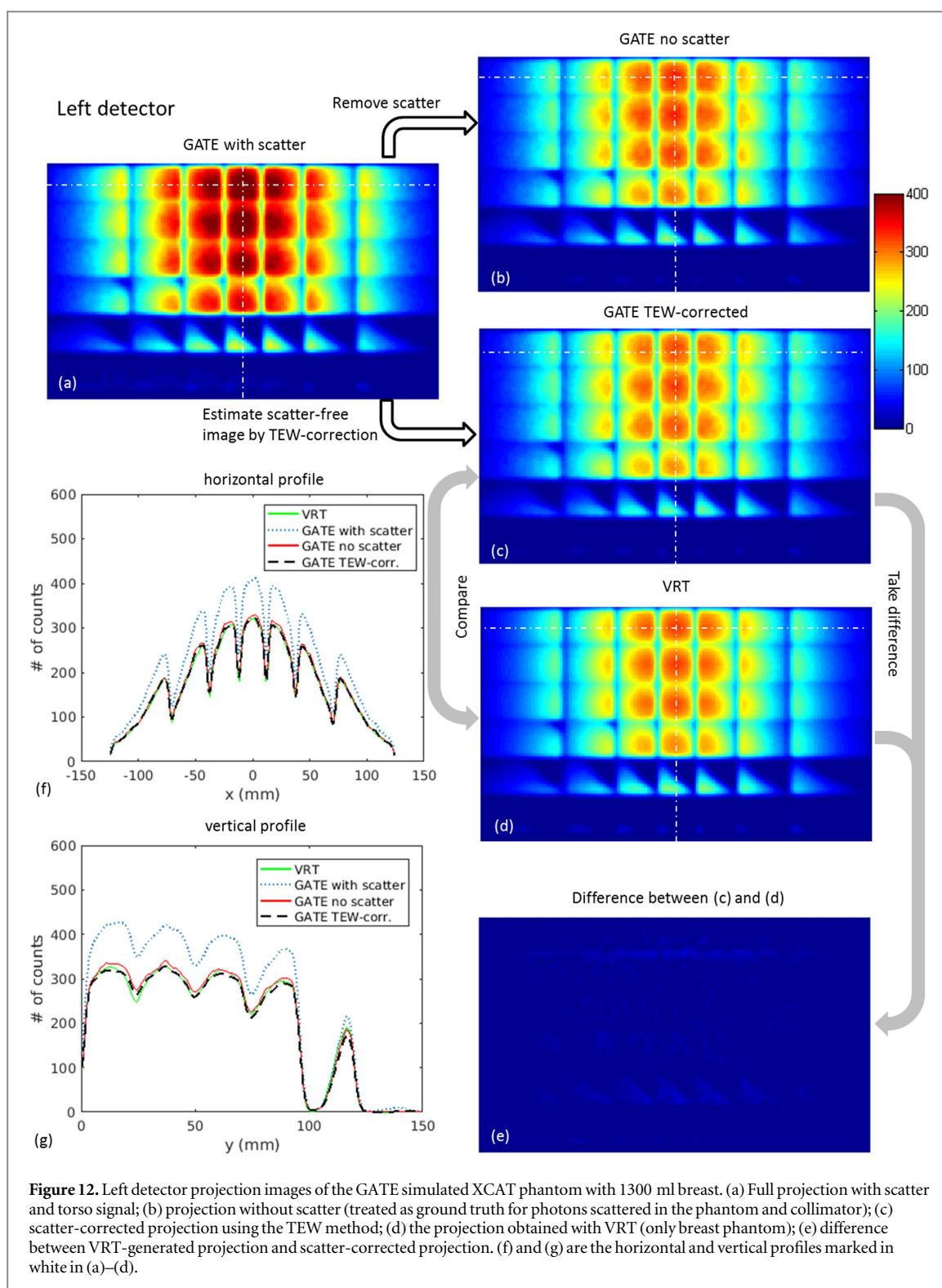


Figure 12. Left detector projection images of the GATE simulated XCAT phantom with 1300 ml breast. (a) Full projection with scatter and torso signal; (b) projection without scatter (treated as ground truth for photons scattered in the phantom and collimator); (c) scatter-corrected projection using the TEW method; (d) the projection obtained with VRT (only breast phantom); (e) difference between VRT-generated projection and scatter-corrected projection. (f) and (g) are the horizontal and vertical profiles marked in white in (a)–(d).

dominates the simulation time. We have shown that with the optimal coarse voxel size, VRT could reach the same difference level from the reference PSFs 337 times faster than accelerated GATE or 29 300 times faster than a full GATE MCS.

Note that the VRT voxel size combination of 1/8 mm and 2 mm is ‘optimal’ for the current collimator and detector geometry. For a different collimator or scanner,

there might be better combinations. However, from our experience, as long as the thickness of the collimator/shielding plate is an integer multiple of the coarse voxel size, and the pinhole diameter does not change very much, the optimal dual grid setting should stay the same. Furthermore, up to now, we have only tried a dual-grid collimator representation. It is possible to use full octree-structure grids to represent the collimator which may lead

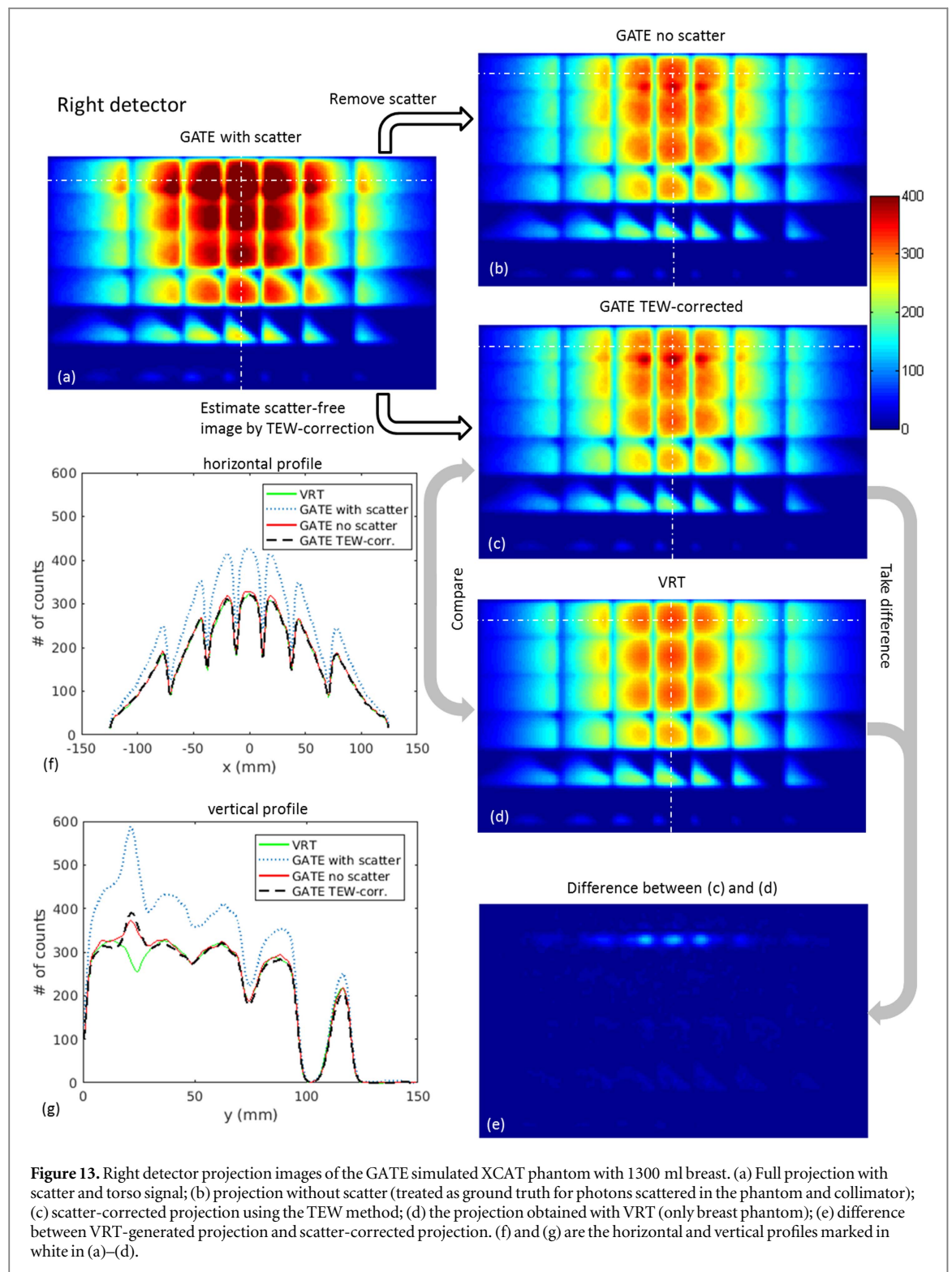


Figure 13. Right detector projection images of the GATE simulated XCAT phantom with 1300 ml breast. (a) Full projection with scatter and torso signal; (b) projection without scatter (treated as ground truth for photons scattered in the phantom and collimator); (c) scatter-corrected projection using the TEW method; (d) the projection obtained with VRT (only breast phantom); (e) difference between VRT-generated projection and scatter-corrected projection. (f) and (g) are the horizontal and vertical profiles marked in white in (a)–(d).

Table 4. Comparison of projection images.

Projection image	Difference	
	NRMSE	Max. difference
400 ml left	1.08%	5.26%
400 ml right	2.44%	15.08%
1300 ml left	1.37%	8.53%
1300 ml right	2.43%	32.85%

to higher time-efficiencies. However, finding the optimal setting for a multi-grid approach is beyond the scope of this research, since the time-efficiency for VRT with the current setting is already good enough for us as with these settings, as noiseless system matrices could be generated in minutes. Compared with other raytracing SPECT simulators in which collimators are defined by analytical shapes (Smith *et al* 1997, Schramm *et al* 2003, Li *et al* 2009, Feng *et al* 2010, Goorden *et al* 2011), the advantage

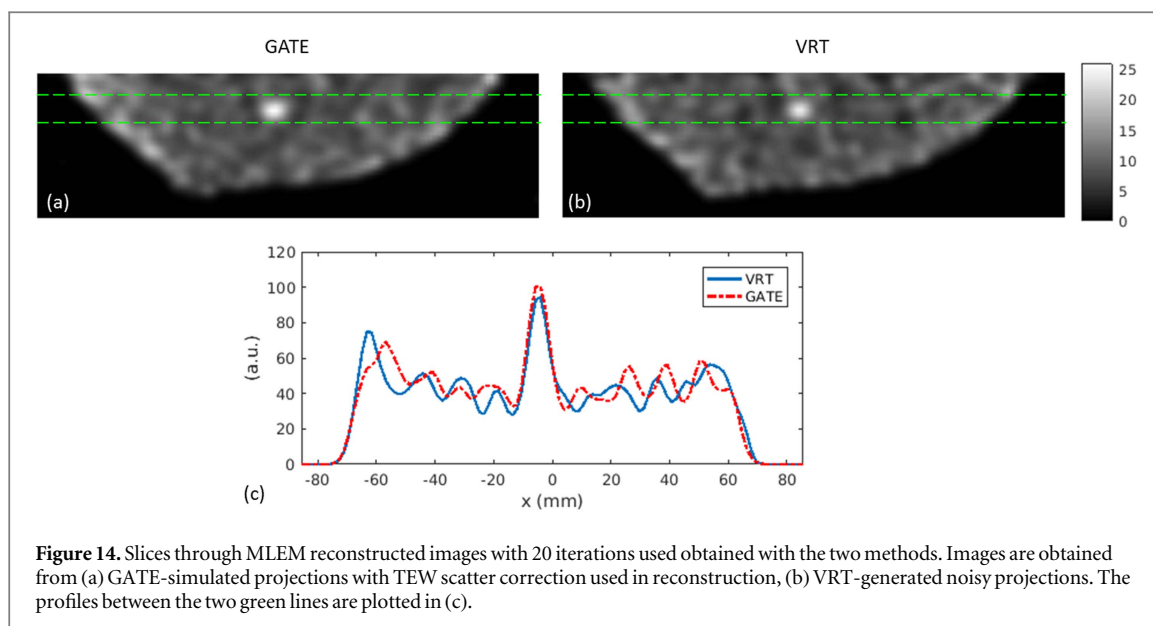


Figure 14. Slices through MLEM reconstructed images with 20 iterations used obtained with the two methods. Images are obtained from (a) GATE-simulated projections with TEW scatter correction used in reconstruction, (b) VRT-generated noisy projections. The profiles between the two green lines are plotted in (c).

Table 5. Reconstructed image comparison.

	GATE	VRT
Contrast	1.36 ± 0.20	1.40 ± 0.24
Noise	0.193 ± 0.015	0.200 ± 0.011

of VRT is that geometries that are hard to describe analytically can be easily implemented. Furthermore, a design drawing of a collimator can be directly voxelized to a volume that can be used in raytracing. The disadvantage is that it requires some trial and error to determine the voxel size (combination) that provides a satisfactory discretisation error and acceptable computational speed.

While the PSF simulations show that in principle VRT is an accurate and fast simulator, they do not consider scattered gamma photons from the human body which can play a major role in clinical imaging and are ignored in VRT. In real scanners, projection images contain scattered photons which are usually corrected for prior to reconstruction or in the iterative reconstruction process. The TEW method is a simple and popular scatter estimation method. Thus, to accurately predict the performance of a real MP-MBT system, the projection images from VRT are supposed to closely resemble TEW-corrected images. In the projection images and profiles in figures 9 and 10, we show that for the 400 ml breast, TEW-corrected GATE projections and VRT projections are very similar, and an NRMSE of about 1% is found. However, for the 1300 ml breast, a discrepancy is encountered. A comparison with scatter-free GATE projections reveals that the discrepancy is not due to scatter (as TEW-corrected GATE images very closely resemble scatter-free GATE images). In

figure 15(a), a zoom-in view of figure 1, it can be seen that some gamma photons from the liver directly reach the right detector through the first row of pin-holes. We checked this by removing the torso phantom and acquiring the same projection image as in figure 13. In the vertical profile of this projection, shown in figure 15(b), the VRT generated profile agrees very well with the scatter-corrected GATE-generated profile. On the left detector, such an issue is not observed as there is no organ on the cranial side of the body that has ^{99m}Tc -Sestamibi uptake as high as the liver. Note that in principle VRT can simulate direct activity from the torso so this finding does not disqualify VRT as an accurate simulator of MP-MBT. However, in this paper we only simulate photons originating from the breast. Thus, the lesson learnt is that when designing such a system one has to consider direct paths from the torso to the detector, and these have either to be taken into account in the simulator or the geometry has to be adapted as to avoid these paths.

As stated above, neglecting Compton scattering in VRT is acceptable with our specified MP-MBT geometry as Compton-scattered photons can be corrected for with a TEW method even though we use a conventional NaI(Tl) gamma detector with a moderate energy resolution of 9%. This minor contribution of Compton scattering to breast images agrees with an earlier work on planar compressed breast imaging with a parallel hole collimator (Hruska and O'Connor 2008a) although other papers have indicated different results (Pani *et al* 1998, Williams *et al* 2003). The reason for the rather small ratio of scattered photons in the photopeak despite the high tracer uptake in the heart and liver probably lies in the fact that gamma photons from the torso have to

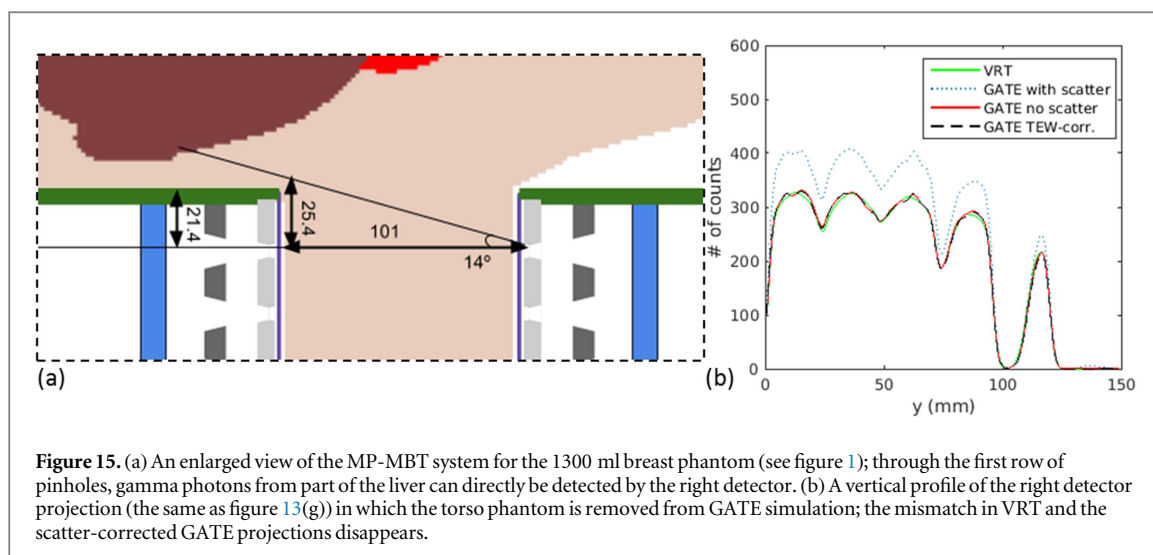


Figure 15. (a) An enlarged view of the MP-MBT system for the 1300 ml breast phantom (see figure 1); through the first row of pinholes, gamma photons from part of the liver can directly be detected by the right detector projection (the same as figure 13(g)) in which the torso phantom is removed from GATE simulation; the mismatch in VRT and the scatter-corrected GATE projections disappears.

be scattered by a rather large angle in order to be redirected in the direction of the gamma detector. Large-angle scatter is generally associated with a large energy loss and thus the majority of these scattered photons can be rejected because they are detected outside the photopeak window. Although in many studies nowadays semiconductor detectors are used, it is shown here that the energy resolution of NaI(Tl) is sufficient for this application.

Note that the fact that VRT can accurately simulate TEW-corrected projections means that we can correct for the bias caused by scatter. However, there is another aspect to scatter that VRT cannot correct for which is the added noise level due to the scattered photons. Therefore, we also simulated reconstructed images based on either GATE-simulated projection or VRT-generated images. Visual inspection as well as contrast-noise characteristics show that images obtained with both methods were very similar, further indicating that VRT can be used to predict the quality of simulated images. As computation time for such images is considerable we only simulated reconstructed images for the 400 ml breast size, but as the scatter fraction is similar for the larger breast our results indicate that the neglect of scatter in VRT is also acceptable for these larger breast sizes. However, in the case larger breast simulation, direct paths from liver to detector either have to be modelled in image reconstruction or prevented by a slight change in design. Note that on the left side of the reconstructed breast images from GATE, there is a slight increase of signal compared to VRT images. We believe that such bias can be removed by tuning the size of the scatter windows and the amount of blurring of the scatter projections. This, however, is beyond the scope of this paper because we have just tested one setting of these parameters, but may be the subject of future research. We chose TEW for scatter correction

because of its simplicity and because it is one of the most commonly used approaches in the clinic (Zaidi and Koral 2004, Hutton *et al* 2011). There are of course other more advanced scatter estimation techniques (Hutton *et al* 2011), which can also be implemented in practice. However, in this paper, we focus on proving that VRT can be used to generate realistic simulated images and testing out different scatter correction techniques is beyond the scope of this paper.

5. Conclusion

VRT can accurately simulate the proposed MP-MBT system with more than four orders of magnitude better time-efficiency than full MCS. Ignoring scatter in VRT is feasible because the amount of scatter in the photopeak is limited in our pinhole collimator-based MP-MBT geometry and can thus be corrected. However, direct gamma photon paths between the liver and the gamma detector can exist for large breast sizes and have to be carefully considered in design and simulation. VRT can be very useful in evaluating geometries for MP-MBT.

Acknowledgments

We thank Dr Paul Segars for kindly providing the XCAT phantom for this research. This work is supported by the Dutch Organization for Scientific Research (NWO) under the VIDI grant ‘Focused imaging of tumors’.

Appendix

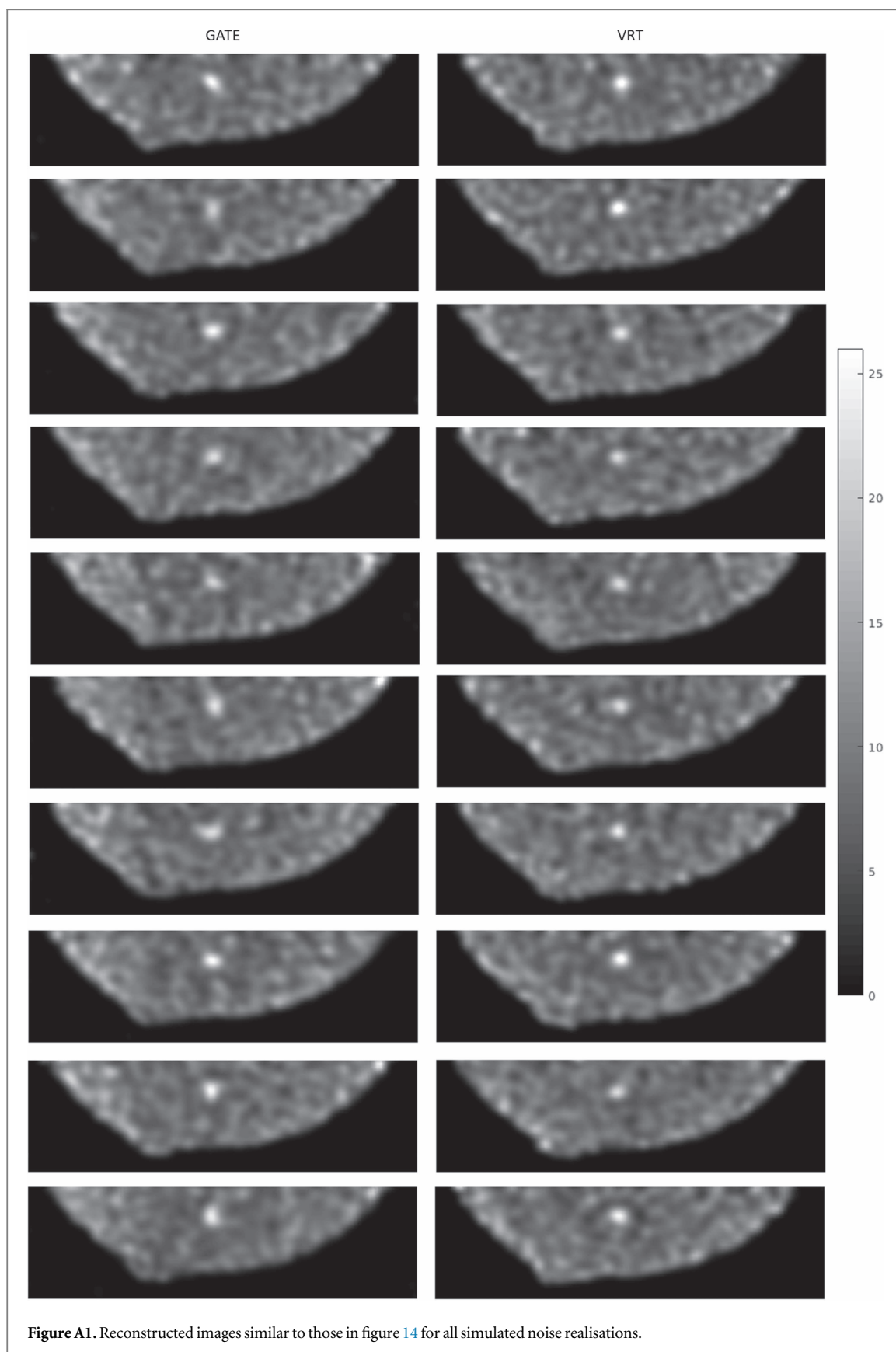


Figure A1. Reconstructed images similar to those in figure 14 for all simulated noise realisations.

References

- Assie K, Gardin I, Vera P and Buvat I 2005 Validation of the Monte Carlo simulator GATE for indium-111 imaging *Phys. Med. Biol.* **50** 3113–25
- Badal A, Kyprianou I, Banh D P, Badano A and Sempau J 2009 penMesh-Monte Carlo radiation transport simulation in a triangle mesh geometry *IEEE Trans. Med. Imaging* **28** 1894–901
- Baghaei H, Li H D, Zhang Y X, Ramirez R A, Wang C, An S H, Liu S T and Wong W H 2010 A breast phantom lesion study

- with the high resolution transformable HOTPET camera *IEEE Trans. Nucl. Sci.* **57** 2504–9
- Beekman F J 2011 Gamma radiation imaging apparatus *US Patent* 20110158384, EP 2310876
- Beekman F J, de Jong H W A M and Slijpen E T P 1999 Efficient SPECT scatter calculation in non-uniform media using correlated Monte Carlo simulation *Phys. Med. Biol.* **44** N183–92
- Bert J et al 2013 Geant4-based Monte Carlo simulations on GPU for medical applications *Phys. Med. Biol.* **58** 5593–611
- Brunner F C, Khoury R, Benoit D, Meessen C, Bonissent A and Morel C 2009 Simulation of PIXSCAN, a photon counting micro-CT for small animal imaging *J. Instrum.* **4** P05012
- Brzymialkiewicz C N, Tornai M P, McKinley R L and Bowshe J E 2005 Evaluation of fully 3D emission mammothography with a compact cadmium zinc telluride detector *IEEE Trans. Med. Imaging* **24** 868–77
- Campbell D L and Peterson T E 2014 Simulation study comparing high-purity germanium and cadmium zinc telluride detectors for breast imaging *Phys. Med. Biol.* **59** 7059–79
- Chen Y, Liu B, O'Connor J M, Didier C S and Glick S J 2009 Characterization of scatter in cone-beam CT breast imaging: comparison of experimental measurements and Monte Carlo simulation *Med. Phys.* **36** 857–69
- Coover L R, Caravaglia G and Kuhn P 2004 Scintimammography with dedicated breast camera detects and localizes occult carcinoma *J. Nucl. Med.* **45** 553–8
- Cot A, Sempau J, Pareto D, Bullich S, Pavia J, Calvino F and Ros D 2002 Evaluation of the geometric, scatter, and septal penetration components in fan-beam collimators using Monte Carlo simulation *IEEE Trans. Nucl. Sci.* **49** 12–6
- Cot A, Sempau J, Pareto D, Bullich S, Pavia J, Calvino F and Ros D 2004 Study of the point spread function (PSF) for I-123 SPECT imaging using Monte Carlo simulation *Phys. Med. Biol.* **49** 3125–36
- De Beenhouwer J, Staelens S, Kruecker D, Ferrer L, D'Asseler Y, Lemahieu I and Rannou F R 2007 Cluster computing software for GATE simulations *Med. Phys.* **34** 1926–33
- de Jong H W A M, Slijpen E T P and Beekman F J 2001 Acceleration of Monte Carlo SPECT simulation using convolution-based forced detection *IEEE Trans. Nucl. Sci.* **48** 58–64
- Descourt P, Carlier T, Du Y, Song X, Buvat I, Frey E C, Bardies M, Tsui B M W and Visvikis D 2010 Implementation of angular response function modeling in SPECT simulations with GATE *Phys. Med. Biol.* **55** N253–66
- Devries D J, Moore S C, Zimmerman R E, Mueller S P, Friedland B and Lanza R C 1990 Development and Validation of a Monte-Carlo simulation of photon transport in an anger camera *IEEE Trans. Med. Imaging* **9** 430–8
- El Bitar Z, Bekaert V and Brasse D 2011 Acceleration of fully 3D Monte Carlo based system matrix computation for image reconstruction in small animal SPECT *IEEE Trans. Nucl. Sci.* **58** 121–32
- Feng B, Chen M, Bai B, Smith A M, Austin D W, Mintzer R A, Osborne D and Gregor J 2010 Modeling of the point spread function by numerical calculations in single-pinhole and multipinhole SPECT reconstruction *IEEE Trans. Nucl. Sci.* **57** 173–80
- Fowler A M 2014 A molecular approach to breast imaging *J. Nucl. Med.* **55** 177–80
- Funk T, Kirch D L, Sun M S, Izaguirre E W, Koss J E, Prevrhal S and Hasegawa B H 2006 Simulation and validation of point spread functions in pinhole SPECT imaging *IEEE Trans. Nucl. Sci.* **53** 2729–35
- Garcia M-P, Bert J, Benoit D, Bardies M and Visvikis D 2016 Accelerated GPU based SPECT Monte Carlo simulations *Phys. Med. Biol.* **61** 4001
- Gieles M, de Jong H W A M and Beekman F J 2002 Monte Carlo simulations of pinhole imaging accelerated by kernel-based forced detection *Phys. Med. Biol.* **47** 1853–67
- Glassner A S 1984 Space subdivision for fast ray tracing *IEEE Comput. Graph.* **4** 15–22
- Goertzen A L, Beekman F J and Cherry S R 2002 Effect of phantom voxelization in CT simulations *Med. Phys.* **29** 492–8
- Gong Z Y and Williams M B 2015 Comparison of breast specific gamma imaging and molecular breast tomosynthesis in breast cancer detection: evaluation in phantoms *Med. Phys.* **42** 4250–9
- Goorden M C, van der Have F, Kreuger R and Beekman F J 2011 An efficient simulator for pinhole imaging of PET isotopes *Phys. Med. Biol.* **56** 1617–34
- Gopan O, Gilland D, Weisenberger A, Kross B and Welch B 2014 Molecular imaging of the breast using a variable-angle slant-hole collimator *IEEE Trans. Nucl. Sci.* **61** 1143–52
- Grevillot L, Frisson T, Maneval D, Zahra N, Badel J N and Sarrut D 2011 Simulation of a 6 MV Elekta precise linac photon beam using GATE/GEANT4 *Phys. Med. Biol.* **56** 903–18
- Gruber G J, Moses W W and Derenzo S E 1999 Monte Carlo simulation of breast tumor imaging properties with compact, discrete gamma cameras *IEEE Trans. Nucl. Sci.* **46** 2119–23
- Hashimoto J, Kubo A, Ogawa K, Amano T, Fukuuchi Y, Motomura N and Ichihara T 1997 Scatter and attenuation correction in technetium-99m brain SPECT *J. Nucl. Med.* **38** 157–62
- Haynor D R, Harrison R L, Lewellen T K, Bice A N, Anson C P, Gillispie S B, Miyaoka R S, Pollard K R and Zhu J B 1990 Improving the efficiency of emission tomography simulations using variance reduction techniques *IEEE Trans. Nucl. Sci.* **37** 749–53
- Hruska C B and O'Connor M K 2006 CZT detectors: how important is energy resolution for nuclear breast imaging *Phys. Medica* **21** 72–5
- Hruska C B and O'Connor M K 2008a A Monte Carlo model for energy spectra analysis in dedicated nuclear breast imaging *IEEE Trans. Nucl. Sci.* **55** 491–500
- Hruska C B and O'Connor M K 2008b Quantification of lesion size, depth, and uptake using a dual-head molecular breast imaging system *Med. Phys.* **35** 1365–76
- Hruska C B and O'Connor M K 2013 Nuclear imaging of the breast: translating achievements in instrumentation into clinical use *Med. Phys.* **40** 050901
- Hruska C B, Phillips S W, Whaley D H, Rhodes D J and O'Connor M K 2008c Molecular breast imaging: use of a dual-head dedicated gamma camera to detect small breast tumors *Am. J. Roentgenol.* **191** 1805–15
- Hruska C B, Weinmann A L and O'Connor M K 2012a Proof of concept for low-dose molecular breast imaging with a dual-head CZT gamma camera. Part I. Evaluation in phantoms *Med. Phys.* **39** 3466–75
- Hruska C B, Weinmann A L, Skjerseth C M T, Wagenaar E M, Connors A L, Tortorelli C L, Maxwell R W, Rhodes D J and O'Connor M K 2012b Proof of concept for low-dose molecular breast imaging with a dual-head CZT gamma camera: II. Evaluation in patients *Med. Phys.* **39** 3476–83
- Hubert-Tremblay V, Archambault L, Tubic D, Roy R and Beaulieu L 2006 Octree indexing of DICOM images for voxel number reduction and improvement of Monte Carlo simulation computing efficiency *Med. Phys.* **33** 2819–31
- Huesman R H, Klein G J, Moses W W, Qi J Y, Reutter B W and Virador P R G 2000 List-mode maximum-likelihood reconstruction applied to positron emission mammography (PEM) with irregular sampling *IEEE Trans. Med. Imaging* **19** 532–7
- Hunter W C J, Barrett H H, Muzi J P, McDougald W, MacDonald L R, Miyaoka R S and Lewellen T K 2013 SCOUT: a fast Monte-Carlo modeling tool of scintillation camera output *Phys. Med. Biol.* **58** 3581–98
- Hutton B F, Buvat I and Beekman F J 2011 Review and current status of SPECT scatter correction *Phys. Med. Biol.* **56** R85–112
- Ichihara T, Ogawa K, Motomura N, Kubo A and Hashimoto S 1993 Compton scatter compensation using the triple-energy window method for single-isotope and dual-isotope spect *J. Nucl. Med.* **34** 2216–21

- Jan S *et al* 2011 GATE V6: a major enhancement of the GATE simulation platform enabling modelling of CT and radiotherapy *Phys. Med. Biol.* **56** 881–901
- Jan S *et al* 2004 GATE: a simulation toolkit for PET and SPECT *Phys. Med. Biol.* **49** 4543–61
- Lamare F, Turzo A, Bizais Y, Le Rest C C and Visvikis D 2006 Validation of a Monte Carlo simulation of the Philips Allegro/GEMINI PET systems using GATE *Phys. Med. Biol.* **51** 943–62
- Li C M, Segars W P, Tourassi G D, Boone J M and Dobbins J T 2009 Methodology for generating a 3D computerized breast phantom from empirical data *Med. Phys.* **36** 3122–31
- Li X and Furenlid L R 2014 A SPECT system simulator built on the SolidWorks™ 3D design package *Proc. SPIE* **9214** 92140G
- Lin J Y, Kench P L, Gregoire M C and Meikle S R 2010 Projection process modelling for iterative reconstruction of pinhole SPECT *IEEE Trans. Nucl. Sci.* **57** 2578–86
- Lippuner J and Elbakri I A 2011 A GPU implementation of EGSnrc's Monte Carlo photon transport for imaging applications *Phys. Med. Biol.* **56** 7145–62
- Ljungberg M, Larsson A and Johansson L 2005 A new collimator simulation in SIMIND based on the delta-scattering technique *IEEE Trans. Nucl. Sci.* **52** 1370–5
- Long Z, Connors A L, Hunt K N, Hruska C B and O'Connor M K 2016 Performance characteristics of dedicated molecular breast imaging systems at low doses *Med. Phys.* **43** 3062–70
- MacDonald L, Edwards J, Lewellen T, Haseley D, Rogers J and Kinahan P 2009 Clinical imaging characteristics of the positron emission mammography camera: PEM flex solo II *J. Nucl. Med.* **50** 1666–75
- Matej S and Lewitt R M 1996 Practical considerations for 3D image reconstruction using spherically symmetric volume elements *IEEE Trans. Med. Imaging* **15** 68–78
- Maublant J *et al* 1996 Technetium-99m-sestamibi uptake in breast tumor and associated lymph nodes *J. Nucl. Med.* **37** 922–5
- Meagher D 1982 Geometric modeling using octree encoding *Comput. Vision Graph.* **19** 129–47
- Moliner L *et al* 2012 Design and evaluation of the MAMMI dedicated breast PET *Med. Phys.* **39** 5393–404
- Mueller B, O'Connor M K, Blevins I, Rhodes D J, Smith R, Collins D A and Phillips S W 2003 Evaluation of a small cadmium zinc telluride detector for scintimammography *J. Nucl. Med.* **44** 602–9
- Ogawa K, Harata Y, Ichihara T, Kubo A and Hashimoto S 1991 A practical method for position-dependent Compton-scatter correction in single photon-emission CT *IEEE Trans. Med. Imaging* **10** 408–12
- Ogawa K and Maeda S 1995 A Monte Carlo method using octree structure in photon and electron transport *IEEE Trans. Nucl. Sci.* **42** 2322–6
- Pani R, De Vincentis G, Scopinaro F, Pellegrini R, Soluri A, Weinberg I N, Pergola A, Scafe R and Trotta G 1998 Dedicated gamma camera for single photon emission mammography (SPEM) *IEEE Trans. Nucl. Sci.* **45** 3127–33
- Perez K L, Cutler S J, Madhav P and Tornai M P 2010 Characterizing the contribution of cardiac and hepatic uptake in dedicated breast SPECT using tilted trajectories *Phys. Med. Biol.* **55** 4721–34
- Raylman R R *et al* 2008 The positron emission mammography/tomography breast imaging and biopsy system (PEM/PET): design, construction and phantom-based measurements *Phys. Med. Biol.* **53** 637–53
- Rehfeld N S, Stute S, Apostolakis J, Soret M and Buvat I 2009 Introducing improved voxel navigation and fictitious interaction tracking in GATE for enhanced efficiency *Phys. Med. Biol.* **54** 2163–78
- Rogers D W O 2006 Fifty years of Monte Carlo simulations for medical physics *Phys. Med. Biol.* **51** R287–301
- Sarrut D and Guigues L 2008 Region-oriented CT image representation for reducing computing time of Monte Carlo simulations *Med. Phys.* **35** 1452–63
- Schmidtlein C R *et al* 2006 Validation of GATE Monte Carlo simulations of the GE advance/discovery LS PET scanners *Med. Phys.* **33** 198–208
- Schramm N U, Ebel G, Engeland U, Schurrat T, Behe M and Behr T M 2003 High-resolution SPECT using multipinhole collimation *IEEE Trans. Nucl. Sci.* **50** 315–20
- Segars W P, Sturgeon G, Mendonca S, Grimes J and Tsui B M W 2010 4D XCAT phantom for multimodality imaging research *Med. Phys.* **37** 4902–15
- Segars W P and Tsui B M W 2009 MCAT to XCAT: the evolution of 4D computerized phantoms for imaging research *Proc. IEEE* **97** 1954–68
- Siddon R L 1985 Fast calculation of the exact radiological path for a 3-dimensional CT Array *Med. Phys.* **12** 252–5
- Siman W and Kappadath S C 2012 Performance characteristics of a new pixelated portable gamma camera *Med. Phys.* **39** 3435–44
- Smith M F, Jaszczak R J, Wang H L and Li J Y 1997 Lead and tungsten pinhole inserts for I-131 SPECT tumor imaging: experimental measurements and photon transport simulations *IEEE Trans. Nucl. Sci.* **44** 74–82
- Staelens S, Vunckx K, De Beenhouwer J, Beekman F, D'Asseler Y, Nuyts J and Lemahieu I 2006 GATE simulations for optimization of pinhole imaging *Nucl. Instrum. Meth. A* **569** 359–63
- Suganuma R and Ogawa K 2000 Effective description of a 3D object for photon transportation in Monte Carlo simulation *IEEE Trans. Nucl. Sci.* **47** 1024–9
- Tabary J, Guillemaud R, Mathy F, Gliere A and Hugonnard P 2004 Combination of high resolution analytically computed uncollided flux images with low resolution Monte Carlo computed scattered flux images *IEEE Trans. Nucl. Sci.* **51** 212–7
- Tornai M P, Bowsher J E, Jaszczak R J, Pieper B C, Greer K L, Hardenbergh P H and Coleman R E 2003 Mammotomography with pinhole incomplete circular orbit SPECT *J. Nucl. Med.* **44** 583–93
- van der Laan D J, Schaart D R, Maas M C, Beekman F J, Bruyndonckx P and van Eijk C W E 2010 Optical simulation of monolithic scintillator detectors using GATE/GEANT4 *Phys. Med. Biol.* **55** 1659–75
- van Roosmalen J, Goorden M C and Beekman F J 2016 Molecular breast tomosynthesis with scanning focus multi-pinhole cameras *Phys. Med. Biol.* **61** 5508
- Vastenhout B and Beekman F 2007 Submillimeter total-body murine imaging with U-SPECT-I *J. Nucl. Med.* **48** 487–93
- Wackers F J T *et al* 1989 Technetium-99m Hexakis 2-Methoxyisobutyl isonitrile—human biodistribution, dosimetry, safety, and preliminary comparison to Tl-201 for myocardial perfusion imaging *J. Nucl. Med.* **30** 301–11
- Wang H L, Jaszczak R J and Coleman R E 1993 A new composite model of objects for Monte-Carlo simulation of radiological imaging *Phys. Med. Biol.* **38** 1235–62
- Wang H L, Scarfone C, Greer K L, Coleman R E and Jaszczak R J 1997 Prone breast tumor imaging using vertical axis-of-rotation (VAOR) SPECT: an initial study *IEEE Trans. Nucl. Sci.* **44** 1271–6
- Williams M B, Judy P G, Gunn S and Majewski S 2010 Dual-modality breast tomosynthesis *Radiology* **255** 191–8
- Williams M B, Narayanan D, More M J, Goodale P J, Majewski S and Kieper D A 2003 Analysis of position-dependent Compton scatter in scintimammography with mild compression *IEEE Trans. Nucl. Sci.* **50** 1643–9
- Yanagida T *et al* 2010 Development of Pr:LuAG scintillator array and assembly for positron emission mammography *IEEE Trans. Nucl. Sci.* **57** 1492–5
- Zaidi H and Koral K F 2004 Scatter modelling and compensation in emission tomography *Eur. J. Nucl. Med. Mol. Imaging* **31** 761–82
- Zbijewski W and Beekman F J 2006 Comparison of methods for suppressing edge and aliasing artefacts in iterative x-ray CT reconstruction *Phys. Med. Biol.* **51** 1877–89